To the Graduate Council:

I am submitting herewith a dissertation written by Ronaldo Minniti entitled "Electron Emission in Grazing Ion-Surface Collisions". I have examined the final copy of this dissertation for form and content and recommend that it be accepted in partial fulfillment of the requirements for the degree of Doctor of Philosophy, with a major in Physics.

Dr. Stuart B. Elston, Major Professor

We have read this dissertation
and recommend its acceptance:

Accepted for the Council:

Associate Vice Chancellor
and Dean of the Graduate School

Electron Emission in Grazing Ion-Surface Collisions

A Dissertation

Presented for the

Doctor of Philosophy

Degree

The University of Tennessee, Knoxville

Ronaldo Minniti

December 1997

Dedication

I want to dedicate this work to my daughter Melissa and my wife Leticia.

Acknowledgments

During my years as a Ph.D. student I interacted with a number of persons at different stages during this project. They have always been available to answer questions or to help in many different ways. I am deeply grateful to all of them.

I want to especially thank my main advisor Dr. Stuart Elston for his help in all the aspects of this work and for sharing his knowledge with me through these years. I have been a student of Dr. Marianne Breinig and Dr. Joachim Burgdörfer in their courses and since then I have frequently consulted them about many aspects of my dissertation work. I am very grateful for their knowledgeable and stimulating advise. I am also very grateful to Dr. Carlos Reinhold for the frequent consultation about theoretical aspects related to this work and for the clarity of his explanations, and to Dr. Ivan Sellin for his advise and cooperation during these years.

I want to thank other members of the atomic physics group who have helped during experimental runs or in other different ways: Leticia Pibida, Ralf Wehlitz, Jon Yong Lim, Henning Lebius, Lee Straus and Stefan Deutscher.

A want to express my appreciation to Mr. Frank Spencer from the machine shop and to the secretaries of the physics department especially to Mrs. Frances Cole (secretary of the atomic physics group) and Mrs. Judy Hutchins. I also want to thank the staff of the EN-Tandem accelerator facility at Oak Ridge National Laboratory for providing the beams used in these experiments.

I am forever grateful to my wife Leticia not only for her invaluable contribution to many aspects of this work but also for her love, support and understanding during these years. This dissertation is dedicated to her and to my daughter Melissa. I finally want to thank my Licenciate advisor Dr. Ignacio Nemirovsky who first introduced me to the field of atomic physics.

Abstract

An experimental setup has been developed to study electron emission produced in grazing incidence ion-surface collisions. Incoming $C^{q_{in}+}$ ($q_{in} = 1, 2, 3$) ions with energies of approximately 0.5 MeV/amu, produced by the EN Tandem Van de Graaff Facility at the Oak Ridge National Laboratory, were directed towards a silicon(100) surface at grazing angles of incidence between 0.1° and 0.8°. Absolute measurements of electron emission spectra were obtained by performing coincidence measurements between electrons emitted in the interaction and ions scattered from the silicon(100) surface in the specularly reflected direction and in a given outgoing charge state. The electrons emitted from the ion-surface interaction were measured using a 160° spherical sector electron energy analyzer employing a position sensitive detector. Such arrangement permitted simultaneous measurement of the energy and angular distributions of emitted electrons. An electrostatic analyzer in combination with a movable electron multiplier detector was used to measure charge state and angular distributions of ions exiting the collision.

Convoy electrons produced in ion-surface collisions result from electron capture and loss to low-lying continuum states of the projectile and constitute a prominent feature in the electron emission spectrum. The present measurements confirm previously reported surface effects on convoy emission , mainly the shift in angle and energy of the convoy peak. A value for the yield of convoy electrons, restricted to within the full-width at half-maximum of the convoy peak, has been determined from the measured absolute electron emission spectra to be ~ 0.4 electrons per ion, in the present projectile velocity regime. Study of the projectile velocity dependence of the convoy electron yields allowed addressing the origin of convoy emission in ion-surface collisions. It has been found that convoy electrons result from capture of valence as well as core electrons in the silicon surface. This result is in contrast with previous conclusions derived from measurements using SnTe surfaces in that convoy emission

originates mainly from electron capture from Sn and Te core states. The present results thereby suggest that convoy emission in ion-surface collisions is sensitive to the target species.

Contents

List of Figures

1 Introduction

This dissertation studies the emission of electrons produced in fast collisions of ions with surfaces. The ions follow trajectories along which they only interact with atoms in the surface layer. Electron emission spectra can then provide important information about the electronic structure of the surface and detailed information about the collision dynamics. Furthermore, the study of the interaction of ions with surfaces provides an important link between atomic physics and condensed matter physics, since much advantage can be taken of the progress which has been made in understanding electron emission produced by the interaction of fast ions with gas and thin foil targets.

In the context of ion-surface collisions, electron emission is generally separated into two broad categories, depending on how energy is transferred from the projectile to the target electrons. Those categories are kinetic electron emission (KEE) [1, 2] and potential electron emission (PEE) [3]. In KEE, the energy required to ionize a target electron is supplied at the expense of the kinetic energy of the projectile. In the case of PEE, the potential energy brought into the collision by the incoming projectile ion is released through Auger-type processes, leading ultimately to the ejection of a target electron. The projectile velocity plays an important role in determining which of the two mechanisms dominates. At very low projectile velocities, and especially for highly charged ions, PEE is dominant. In fast ion-surface collisions, in contrast, most electron emission results from KEE type processes. The electron emission spectra produced by a fast charged particle interacting with a surface show features resulting from direct ionization of target electrons and from target- or projectile-electron transfer to a projectile continuum state.

There are a large number of surface analytic techniques that employ ions interacting with surfaces. This serves as motivation to better understand the ion surface interaction [4]. The study of ion-surface interactions implicitly requires that the col-

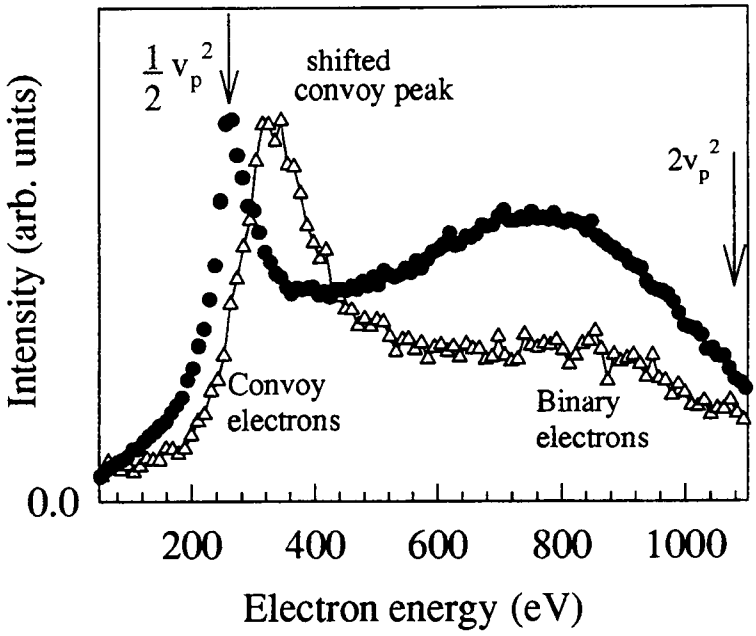

Figure 1.1: Spectra of emitted electrons produced by 6.0 MeV C^{2+} ions incident at a grazing angle of 0.15° upon a silicon surface (hollow symbols) and transmitted through a thin carbon foil (solid symbols).

lision conditions must be carefully chosen to guarantee ion trajectories that glance off the surface and do not penetrate the surface layer and interact with the bulk solid. Such conditions are achieved by utilizing ions that are incident at glancing angles to the solid surface.

In grazing incidence ion-surface collisions, some of the electrons emitted are dramatically affected by the interaction of the ion with the surface. These electrons are emitted in the direction of the ion scattering from the surface *i.e.* into a narrow range of angles around the forward direction. The energy spectrum of forward emitted electrons produced by ions interacting at grazing incidence with a solid surface is shown in Fig. 1.1. Typical features observed in such a spectrum are a tail of low energy electrons (not observed in the figure since they have been suppressed

in the experiment), a broad peak shaped structure called the convoy peak similar to the cusp or convoy peak observed in ion-atom collision and transmission-foil experiments, and a high-energy binary encounter shoulder. Fig. 1.1 also shows the spectrum of forward emitted electrons produced by ions transmitted through a thin carbon foil. As can be observed in the figure the structures produced in ion-foil collisions are strongly altered by the ion-surface interaction. This suggests that electrons emitted in the forward direction become a good probe to study different aspects of the ion-surface interaction.

Convoy electrons, in particular, are most affected by the ion-surface interaction. Convoys are produced by electron capture (ECC) and electron loss (ELC) to continuum states of the projectile. They therefore travel in close proximity to the ion during the course of the collision serving as a good spectator of the interaction of the ion with the surface.

Convoy electron production has been studied extensively in ion-atom collisions and much of the knowledge gained here can be of help in interpreting ion surface collision results. The forward electron spectrum produced in ion-atom collisions displays a cusp shaped peak positioned at $E_{cusp} = \frac{1}{2}v_p^2$ where v_p is the projectile velocity and E_{cusp} is referred to as the cusp energy (All equations presented in this dissertation are expressed in atomic units). Cusp electrons travel with nearly the same velocity as the projectile. The shape of the cusp is determined by the ion-atom interaction under single collision conditions. In the special case of an ion interacting with a solid at grazing incidence the scenario is much more complicated. A single ion encounters many collisions with surface atoms, and an electron transferred to a projectile continuum state interacts with many electrons on its way out of the collision (electron transport) leading to a degradation in energy of these electrons. Furthermore, under grazing incidence conditions, the interaction time between the ion and the surface is very long, leading to a polarization of surface electrons that develops in response to the Coulomb charge of the passing ion. The potential aris-

ing from such polarization has the form of a wake and is called the surface-wake potential. The surface wake potential strongly affects the electron emission in an ion-surface interaction. In particular, this potential results in a repulsive force on an emitted convoy electron. Convoy electrons as well as the surface-wake travel with the projectile ion. Therefore the surface wake potential will interact and modify convoy emission. The peculiar geometry of ions interacting with a surface under grazing incidence therefore provides an ideal scenario to probe physical properties of the ion-surface interaction.

The convoy peak produced in ion-surface collisions is broadened and shifted, often by many tens of eV out of a few hundred of eV, toward higher energy from the projectile velocity-matched value (E_{cusp}) observed in transmission experiments as seen in Fig. 1.1. The first observation of the ion-surface convoy peak was made by De Ferraris and Baragiola [5] for the scattering of protons from an aluminum surface. They observed a broadening of the peak but not a shift. A similar broadening was observed later using a semiconductor surface [6]. A shift of the peak was observed experimentally for the first time by Hasegawa *et al.* [7] and subsequently by other laboratories [8, 9, 10, 11, 12, 13, 14]. Several explanations for the ion-surface peak shift have been proposed [15, 7, 16, 11, 1, 17] and most of them seem to agree that the energy shift results from the interaction between the emitted electron and the surface wake potential that forms in response to the passing Coulomb projectile. An alternative explanation proposed by Baragiola [1] suggests that the cloud of secondary electrons ejected by the fast ion could exert a repulsive force on a convoy electron leading to the shift. However this effect has been estimated to be small [18].

In addition to providing information about the collision dynamics, electron spectra from ion-surface collisions also can provide information on the electronic structure of the surface. The binary encounter electron (BEE) structure observed in Fig. 1.1, contains such information. A BEE results from a quasi elastic two-body collision between the projectile and a target electron. Assuming BEE resulting from an elastic

two-body collision, from conservation of momentum and energy, the velocity of the emitted electrons in the lab frame is given by $v_e = 2v_p \cos\theta$, were v_p is the projectile velocity and θ is the electron emission angle. Consequently binary electrons emitted in the forward direction, $\theta_e \sim 0$, would be ejected with $v_e = 2v_p$. In reality the collision is not a pure elastic two body interaction. The fact that the electron is initially bound to the target and that it has a velocity distribution, leads to a shift of the binary peak to lower electron energy than the expected value of $E_{BEE} = 2v_p^2$ (atomic units) as indicated in Fig. 1.1. The shape of the binary peak is determined by the momentum distribution of the electrons in the target and the variations of the elastic electron-ion scattering cross section with energy and angle. Therefore the study of the binary shoulder, as observed in ion-surface collisions, may provide important information on the wave function of valence electrons in the surface and therefore contribute to the knowledge of the surface electronic structure.

The few theoretical descriptions of electron emission in fast ion surface collisions have mainly focused on explaining the convoy peak shift [7, 10, 11, 19, 17]. Little attention has been paid to the remaining aspects of the forward emission spectrum, in particular the shape of the convoy peak, the angular distribution of the emitted electrons, [18], the shape of the binary encounter shoulder [17, 19, 20], yields or the origin of electrons belonging to different energy regimes of the electron emission spectrum.

Recently, a classical trajectory Monte Carlo (CTMC) simulation of kinetic emission from grazing incidence collisions has been developed [17, 18]. It requires a detailed microscopic description of both core and valence surface electron densities, which affect ionization and capture probabilities, as well as careful treatment of the transport and multiple scattering of electrons near the surface, and the surface image interactions. Comparison of calculated and experimental electron emission spectra produced in collisions of Li ions with SnTe surfaces have found reasonable agreement with the experimental shape of the CEP. However several discrepancies have

been noted -for example, the CEP peak shift is overestimated in the model. It was suggested [21] that a measurement of absolute yields would be a sensitive test of the underlying mechanisms of convoy electron production, such as electron capture from valence and core shells and electron loss to the continuum. In early CTMC simulations [17] it was concluded that in ion-surface collisions convoy electrons were mainly produced by capture of core electrons in the target. But this conclusion may only hold for the particular collision system studied and may change for a different projectile-target combination.

The work forming the basis of this dissertation provides the first measurements of absolute convoy electron yields [14] from grazing collisions of fast carbon ions with a silicon(100) surface. A comparison of measurements of absolute convoy electron yields with theoretical calculations leads to the conclusion that both core and valence electrons from the target contribute to convoy emission and that the relative roles of valence and core electrons in convoy emission is sensitive to the surface species.

Motivated by the great number of challenging questions and unknowns, some of which have been briefly outlined in the above paragraphs, an apparatus has been developed [13, 22] to measure electron emission in grazing ion-surface collisions. The existing apparatus allowed simultaneous measurement of the energy and angular distributions of electrons ejected near the forward direction. For this dissertation modifications were added to permit coincident measurements between the emitted electrons and ions exiting with a particular exit charge state and exit angle. In addition the newly modified apparatus permitted measuring exit charge state and angular distributions of ions scattered from the surface. The design and construction of the ion analysis and coincidence apparatus constituted a major portion of this work.

Energy and angular distributions of electrons have been measured as well as charge state and angular distributions of ions scattered from the surface. The collision system studied consisted of carbon projectile ions with total impact kinetic

energies between 2.4 and 6.0 MeV incident upon a silicon(100) surface. The projectile ions were incident at surface grazing angles between 0.15° and 0.8°.

The remainder of this dissertation is organized in the following way: Chapter 2 discusses theoretical aspects involved in the description of ion-surface interactions. Chapter 3 describes the experimental setup. Chapter 4 focuses on the measurement of angular and charge state distributions of the scattered ions. In chapter 5 results concerning the electron emission are presented. A summary is presented in chapter 6.

2 Theory

2.1 Overview

The study of electron emission in grazing ion-surface collisions is a fascinating problem involving concepts derived from several independent research fields. As a result, the theoretical description of the underlying physical mechanisms becomes a complex matter. This chapter is intended to summarize the main concepts involved in describing electron emission in ion-surface collisions, providing the reader with enough tools to understand discussions appearing in later chapters. Section 2.2 describes quantitatively the conditions that must be imposed on collision parameters for ions to undergo grazing collisions. The following section introduces the concept of the surface wake potential which results from polarization of surface electrons in the presence of an ion traveling near the surface. The last two sections describe convoy and binary electron emission. A brief summary of what is known about the emission in the more simple case of ion-atom collisions is presented as well as modifications to be expected of both structures in the more complicated case of ion-surface collisions.

2.2 Grazing incidence collisions

In order to study ion-surface interactions the projectile ions must interact with the topmost layer of atoms. This is achieved by using glancing angles of incidence. Under grazing incidence the ion encounters many soft collisions with atoms of the surface. As a result, the trajectory of the ion will be determined by a series of small angle quasi-elastic collisions of the incoming ion with each one of these atoms.

In grazing incidence collisions, the interaction potential between the ions and the surface atoms is given by a superposition of atomic potentials. The net effective potential therefore can be represented by a planar averaged interaction potential $V_{plan}(x)$, where x is the distance from the surface. Using such an approximation

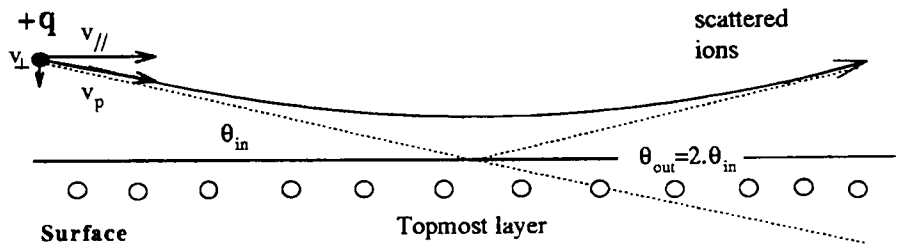

Figure 2.1: Incident ions are specularly reflected from the surface.

for the repulsive potential produced by the surface atoms, the ion moves in a region where the electric field is perpendicular to the surface (since the surface is being considered an infinite sheet with uniform charge density). The trajectory then followed by an ion under grazing incidence is specularly reflected by the surface, as seen in Fig. 2.1, *i.e.* the scattering angle corresponds to $\theta_{out} = 2\theta_{in}$. The above picture assumes that the scattering process is perfectly elastic (*i.e.* energy is conserved) and that the ion doesn't change charge along the trajectory. Fig. 2.1.

At a given angle of incidence fast particles will follow trajectories that get closer to the surface compared to slower particles. It follows then that for a particle, with a given kinetic energy, a critical value for the angle of incidence, θ_{crit}, can be determined to guarantee reflected trajectories. In order to determine θ_{crit}, an expression for V_{planar} must be derived which results from averaging the ion-atom interaction potential over the surface as:

$$V_{plan}(x) = 2\pi n_p \int_0^\infty V_{atom}(\sqrt{x^2 + R^2}) R dR, \qquad (1)$$

where x is the distance of the ion from the surface, n_p the surface atomic density and $V_{atom}(r)$ is the ion-atom interaction potential, approximated here by the screened

Coulomb potential expressed as

$$V_{atom}(r) = \frac{Z_P Z_T}{r} f(r), \tag{2}$$

where f(r) is the screening function. Using the parametrized Moliere screening function for the atomic Coulomb potential [23] equation 1 can be solved and gives

$$V_{plan}(x) = 2\pi n_p Z_P Z_T a_s \sum \frac{c_i}{d_i} \exp(-\frac{d_i x}{a_s}), \tag{3}$$

where $Z_{P,T}$ are the bare nuclear charges of the projectile and surface (target) respectively, a_s is called the screening length and $\{c_i\}$, $\{d_i\}$ are screening parameters. In the Moliere approximation $\{c_i\} = \{0.35, 0.55, 0.1\}$, $\{d_i\} = \{0.3, 1.2, 6\}$ and

$$a_s = 0.88534(Z_P^{\frac{1}{2}} + Z_T^{\frac{1}{2}})^{-\frac{2}{3}}. \tag{4}$$

Fig. 2.2 shows the planar-averaged Moliere interaction potential for a carbon ion interacting with a silicon(100) surface, calculated from equation 3.

The motion of the ion is characterized by the parallel and perpendicular components of the projectile velocity. The energy associated with the perpendicular component of motion, referred to from now on as *perpendicular energy*, can be expressed in terms of the total kinetic energy of the projectile and the incidence angle as

$$E_{perp} = \frac{1}{2} v_{perp}^2 = E_P \sin^2 \theta_{in} \tag{5}$$

where E_P is the total projectile kinetic energy. Equation 5 provides a simple expression to calculate the perpendicular energy of the ion for a given impact energy. To avoid penetrating trajectories the condition $E_{perp} < V_o$ must be satisfied, where V_o represents the height of the potential barrier provided by the surface atoms ($V_o = V_{plan}(x = 0)$). For the particular case of carbon ions interacting with a silicon

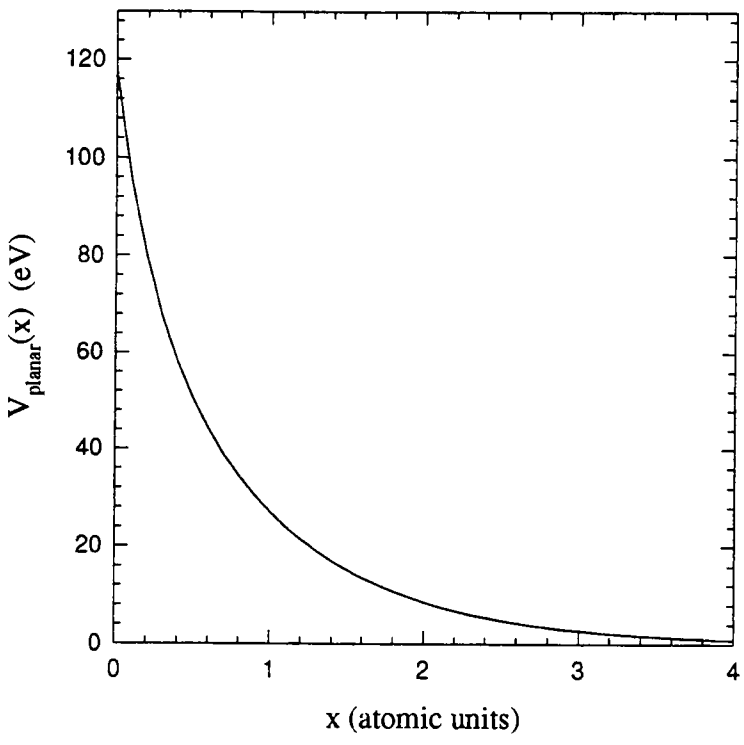

Figure 2.2: Planar potential for carbon ions interacting with a silicon(100) surface.

surface, $V_o \approx 120$ eV. Thus, for example, with 3.6 MeV ions the incident angle must satisfy $\theta_{in} < \theta_{crit} = 0.33°$ to avoid surface penetration.

2.3 Surface-wake potential

Ions interacting with a surface at grazing incidence provide a very interesting scenario to probe physical properties of the surface due to the long interaction time between the ion and the surface. As a result of this peculiar geometry and for microscopically flat surfaces dynamic image interactions become of great importance in describing the energy and angle distributions of charged particles (electrons and scattered ions) during the ion-surface interaction.

As a positive ion approaches a solid surface the ion polarizes the solid resulting

in a rearrangement (or removal) of the electrons in the surface due to the presence of the electric field of the moving ion. The resulting polarization potential induced by the moving ion is called the surface-wake [24, 25, 26, 23] or, alternatively, the dynamical image potential and can be qualitatively understood as follows: In the case of a static ion of charge q at a distance d in front of a solid surface electrons near the surface rearrange to shield the interior from the external field of the ion. The resulting surface induced charge density produces fields external to the surface identical to those that would be produced by the charge q and an image charge of charge $-q$ located at a distance $-d$ from the surface (method of images). When the ion is in motion, the finite characteristic surface electron velocities results in rearrangement that is less than perfectly responsive, and a dynamically evolving negative charge distribution is formed instead which, due to the slower response, lags behind the projectile ion.

The potential as seen by a fast emitted electron resulting from the induced charge density in the surface can be envisioned to first order as the potential produced by a negative image charge lagging behind the ion, as shown in Fig. 2.3.

The resulting induced potential is sometimes referred to as the dynamical image potential. The negative image charge exerts an attractive force on the positive ion and a repulsive force on any electron ejected during the ion surface interaction [15, 16]. (the force exerted by the dynamical image potential on an electron is shown in Fig. 2.3).

A more realistic representation of the induced charge density is given by the surface-wake. Since the perturbation produced by the ion is time dependent the induced surface charge density fluctuates in time resulting in an oscillatory electric field which resembles a wake pattern. This in turn is what gives rise to the name surface-wake potential. Fig. 2.4 shows a calculated surface wake potential [27] experienced by an electron due to a 0.3 MeV/amu proton moving parallel to a SnTe(100) surface as a function of the position vector of the electron (x,1 a.u.,z).

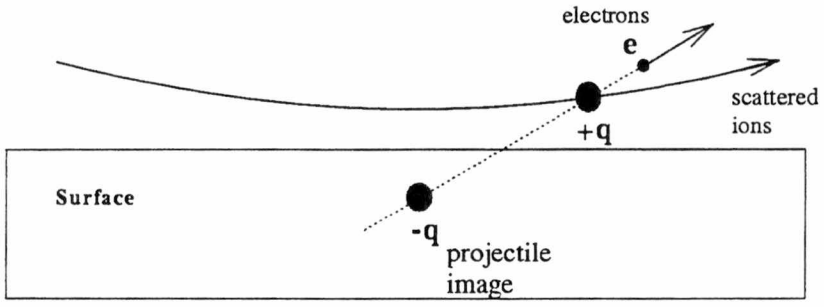

Figure 2.3: Interaction of the ion image charge with an electron in the vicinity of the surface. The image charge acceleration experienced by an ejected electron, due to the image charge of the ion, is indicated by an arrow.

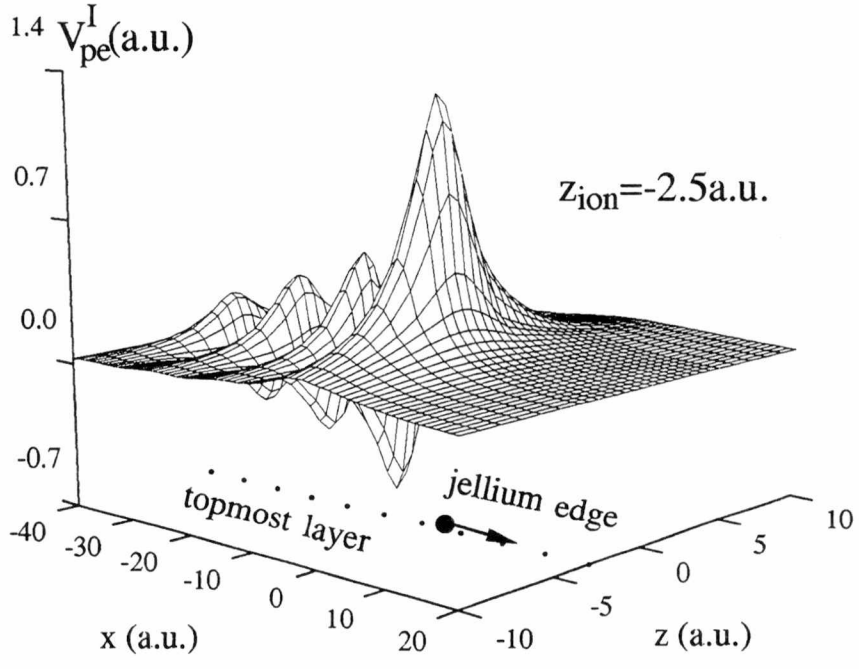

Figure 2.4: Calculated wake potential produced by an 0.3 MeV/amu H^{1+} ion moving parallel to a SnTe surface.

The position of the projectile is ($x = 0$,$y = 0$,$z_i = -2.5$ a.u.) (*i.e.* 0.5 a.u. above the top row of atoms). The position of the maximum amplitude for the first oscillation appears behind the projectile indicating the ion being trailed by the surface-wake. The amplitude of the first oscillation corresponds to a repulsive well which represents the repulsive force exerted by the wake on the electron. Note in addition that the surface wake potential exerts an attractive force on the positive ion . The shift of the convoy peak discussed in the previous chapter results from an acceleration of these electrons by the surface-wake potential. Acceleration of convoy electrons by the surface wake, or dynamical image potential, was discussed for the first time by Burgdörfer [15]. As will be discussed in the following section convoy electrons as well as the surface wake travel with the projectile ion. Therefore the surface wake potential will interact and modify convoy emission [9, 10, 17].

2.4 Convoy electron emission

Convoy electrons have been observed in ion-atom collisions and in ion-foil transmission experiments as a distinct cusp-shaped peak in the forward electron spectrum at electron energies were the electron velocity in the lab frame, v_e, matches the velocity of the projectile v_p [28]. This results from a divergence in the triply differential cross section, $\frac{d\sigma}{d\bar{v_e}}$, expressed as

$$\frac{d\sigma}{d\bar{v_e}} \propto \frac{1}{|\bar{v_e} - \bar{v_p}|}, \tag{6}$$

for electron emission velocities such that $|\vec{v_e} - \vec{v_p}| \longrightarrow 0$. This latter condition implies emission angles within a narrow cone of half angle θ centered about the forward direction (θ corresponds to the spherical coordinate polar angle with the z-axis given by incident projectile direction); typically, $\theta \leq 5°$.

As mentioned in the previous chapter, electrons contributing to the convoy peak result from two KEE processes: Target ionization, in which a target electron is

captured to a projectile continuum state (ECC) and/or projectile ionization, in which an electron is lost to a projectile continuum state (ELC). In both cases, the final state of the electron is a low energy (near threshold) projectile continuum state which is described by a Coulomb wave function [29] in the rest frame of the projectile. It has become recognized [30] that for both ECC and ELC the cusp in the emission spectrum results from the $1/v'_e$ singularity which appears in the low velocity limit of the Coulomb wave normalization factor; here v'_e is the electron velocity in the projectile rest frame.

The above discussion addresses the convoy peak position which results from the fact that electrons travel at nearly the same velocity as the projectile. In addition an electron transferred to a low lying projectile continuum state, *i.e.* a convoy electron, travels in close proximity to the ion. Therefore the shape of the convoy peak is mainly determined by the post collision interaction between the attractive field of the ion and the electron. In the particular case of ECC the screened target nucleus affects, to second order, the shape of the peak which is seen in the electron spectrum as an asymmetry in the low energy tail.

In ion-surface collisions the position and shape of the peak are dramatically affected compared to the case of ion-atom collisions already discussed in connection with Fig. 1.1. The ion-surface convoy peak is broadened and shifted which is caused mainly by the ion induced surface-wake potential introduced in the previous section. Most of the early attempts to describe fast electron emission in ion-surface collisions [9, 10, 11] viewed convoy emission process as a two step process. First, the electron is captured from a bound state to a projectile continuum state and second, the electron is accelerated by the surface wake. Based on this approach Iitaka *et al.* [9] and Kimura *et al.* [10] employed CTMC simulations to calculate the energy distribution of emitted electrons. Both models assume, as initial conditions for the calculations, that the captured electrons are initially uniformly distributed in a sphere centered in the rest frame of the projectile. The electrons then propagate in the combined

field of the projectile and its image. The calculated energy spectra show a shift of the peak due to the image charge acceleration of the convoy electron.

More recently, Reinhold and Burgdörfer [18] have developed a more complete description of the emission of electrons in grazing ion-surface collisions. This model includes realistic initial states for the electrons in the target and projectile. Thus, electron emission is decomposed into contributions arising from capture from initial states that are chosen to reproduce certain characteristics (*e.g.* binding energy) of target core and valence electrons. In further contrast to previous models, the electron is considered, to move in a combined potential composed of four contributions describing: (i) the field of the projectile ii) the dynamic image charge induced by the projectile, iii) the surface barrier potential, and iv) the field of the initial target core. Fig. 2.5 shows the total potential, as seen by an electron near a surface, calculated by Reinhold and Burgdörfer [18]. The calculated potential corresponds to 0.3 MeV/amu Li^{2+} moving parallel to an SnTe(100) surface. The figure clearly displays all four contributions to the total potential. Note that the figure is plotted over a smaller range of values for the coordinate x than in Fig. 2.4, and consequently only one wake oscillation is displayed as opposed to the several wake oscillations that can be observed in Fig. 2.4. An additional important consideration included in the calculation, which was simplified in earlier models, is the treatment of the transport of the electron from it's initial electronic state, through a sequence of multiple scatterings with other electrons, to its final state. This is taken into account by adding a stochastic term in the total Hamiltonian of the system.

The results from the simulation are in quite good agreement when compared to experimental measurements [17, 18, 14]. The calculation reveals that the shifted and broadened convoy peak observed in ion-surface collisions, results from a rainbow scattering of the liberated electrons in the dynamically screened field of the projectile. A picture to keep in mind is that the ion has penetrated the electronic selvage and the field of the ion (which is exerting an attractive force on the electron) is screened by

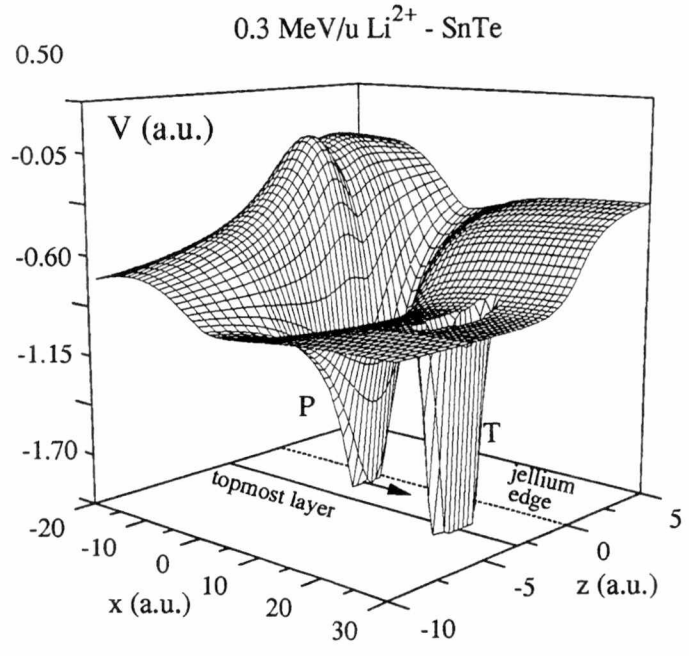

Figure 2.5: Total potential seen by an electron initially in a target core (T) near a 0.3 MeV/amu Li^{2+} ion (P) moving parallel to a SnTe(100) surface.

the polarized surface electrons (which produce the wake) and the field of the target. Therefore in the projectile frame the surface wake potential acts as a screening of the ion's potential and forms part of the total dynamical screened field of the projectile. The convoy peak results from rainbow scattering of the electron in the total screened field of the projectile but the shift is mainly due to the repulsion of the surface wake.

2.5 Binary encounter electron emission

Ionization of target atoms resulting from a head-on collisions of the projectile nucleus with a loosely bound electron (usually an outer shell electron) leads to the ejection of a so-called binary encounter electron (BEE). Expressions for the BEE process derived in the case of ion-atom collisions provide a useful starting point for later discussion

of the more complicated problem of BEEs ejected in ion-surface collisions. Since we are interested in the forward emission spectrum only target BEE will be considered in the following discussion.

From scattering kinematic considerations (*i.e.* applying conservation of momentum and energy to the classical two body problem of a heavy particle colliding elastically with a free light particle) the energy of the ejected electron (or binary encounter peak) is found to be

$$E_{BEE} = 4E_{cusp}\cos^2\theta_{lab} \tag{7}$$

where E_{cusp} corresponds to the cusp energy and is defined as $E_{cusp} \equiv \frac{1}{2}m_e v_p^2$.

The dynamical aspects of the binary encounter process can be described in terms of the triply differential cross section $[\frac{d\sigma}{dEd\Omega}]_{BEE}$. Since the impact parameters involved in the collision between the projectile nucleus and target electron is very small, the interaction can be described by a quasi-elastic scattering process involving only two particles. The problem is nicely described in the center of mass frame (practically the projectile frame) as an electron with velocity $\vec{v}$ (equal to the projectile velocity $-\vec{v}_p$) scattering elastically off the screened Coulomb potential of the projectile ion. For the case of an electron scattering from a bare nucleus, the differential cross section is well known and is described by the Rutherford formula [31] as

$$[\frac{d\sigma}{d\Omega}(\theta)]_{Ruth} = \frac{(Z_P e)e}{16E^2\sin^4(\frac{\theta}{2})}, \tag{8}$$

where Z_P is the bare nuclear charge of the projectile, E is the energy of the free electron *i.e.* $E = \frac{1}{2}v_p^2$, and θ corresponds to the scattering angle in the projectile frame.

The above picture, however, considers the electron to be free in the target. To account for the electron being initially bound, the Rutherford formula can to first

approximation, be convoluted with the momentum distribution $|\psi(\vec{p})|^2$ of the electron in the target. A simple description has been given *e.g.* by Lee *et al.* [32] within the framework of the impulse approximation and leads to an expression for the differential cross section in the projectile frame for the BEE process given by

$$[\frac{d\sigma}{d\Omega}(\theta)]_{BEE} = \int [\frac{d\sigma}{d\Omega}(\theta)]_{Ruth} |\psi(\vec{p})|^2 d^3p, \tag{9}$$

where $[\frac{d\sigma}{d\Omega}]_{Ruth}$ represents the Rutherford scattering cross section of a free electron by a bare projectile ion, and $\psi(\vec{p})$ corresponds to the target-electron wave function. The energy of the electron in the projectile frame now has to account for the electron being bound to the target and is given by

$$E(p) = \frac{(\vec{s}+\vec{p})^2}{2} - E_B, \tag{10}$$

where E_B is the binding energy of the electron and $\vec{s} = m\vec{v}$ is the momentum of the electron in the target. The integral in equation 9 has been solved by Lee *et al.* [32] for the particular case of binary electrons emitted in the forward direction in the lab frame (*i.e.* $\theta = 180°$ in the projectile frame), leading to an expression for the triply differential cross section $[\frac{d\sigma}{d\Omega}(E, \theta = 0°)]^{lab}_{BEE}$ in the lab frame given by

$$[\frac{d\sigma}{d\Omega}(E, \theta = 0°)]^{lab}_{BEE} = \frac{Z_P^2 e^4 J(p_z)}{16E(p_z)(s+p_z)} \sqrt{\frac{E_{lab}}{E}}, \tag{11}$$

where p_z is the component of the momentum parallel to the beam axis. $J(p_z)$ sometimes called the Compton profile of the target electron is given by

$$J(p_z) = \sum_i \int\int dp_{ix} dp_{iy} |\psi_i(\vec{p_i})|^2. \tag{12}$$

Equation 11 provides a simple analytic expression showing explicitly that the shape and position of the binary peak is given by the Compton profile of the ejected electron. This in turn indicates that measurements of the binary peak provide information about the momentum distribution (Compton profile) of valence electrons

in the target.

In ion-surface collisions a comprehensive theoretical description of the binary encounter process [19, 33, 20, 18] is far from complete. Experimentally the ion-surface binary encounter structure is seen as a broad shoulder in the high energy regime of the electron spectrum as opposed to a well-defined peak as seen in ion-atom collisions (see Fig. 1.1). The initial state of a target valence electron is no longer a localized atomic state but rather a state belonging to the band structure of the solid. In addition, electrons originating in a binary encounter process are degraded in energy due to the transport of the electron throughout the surface. These two differences are thought to be responsible for the broadening of the binary encounter electron peak [19, 20, 18]. On the other hand as described in equation 11 the study of the binary encounter structure in ion-surface collisions may provide information about the Compton profile of valence electrons in the surface to the extent the transport problem can be understood.

3 Experimental Setup

3.1 Overview

Carbon ions with charge states from $q = 1$ to $q = 4$ and kinetic energies between 2.4 and 6.0 MeV were produced by the 7.0 MV EN-Tandem Van de Graaff accelerator at Oak Ridge National Laboratory. A (cesium sputter-type) ion source was used to produce negative carbon ions to inject into the tandem accelerator which were then accelerated to a kinetic energy of Ve up to the terminal at voltage V located halfway inside the tank. At the terminal the C^- ions were stripped of their electrons by a gas target and were left with a positive charge q becoming then accelerated away from the terminal by an additional amount of energy qVe. Therefore the total kinetic energy of a positive ion exiting the tank was $E = (q+1)Ve$. The ions exiting the stripper were composed of several different charge states distributed about an average value q_{avg}. An analyzing magnet was used to select the desired charge state. Therefore by adjusting the terminal voltage V and using the analyzing magnet a beam of carbon ions with the desired energy and charge state could be selected.

The beam particles exiting the analyzing magnet were steered through the remaining part of the accelerator beamline into the experimental chamber. Before entering the chamber the beam was collimated by two circular apertures to a diameter of 0.2 mm and an angular divergence of less than 0.015° (half -angle) at the surface target. The upstream and downstream apertures, separated by a distance of 1 meter, were 0.6 and 0.2 mm respectively. Both apertures were electrically isolated to permit measurement of the beam current at those particular places. Typical beam currents on the upstream aperture was $\sim$ 50 nA while maximum beam currents on target were less than 10 pA after collimation. A differential pumping stage connected the accelerator beamline (with a pressure near 1×10^{-8} Torr) to the main UHV experimental chamber, were the pressure was approximately 1×10^{-10} Torr.

Single-crystal silicon (100) targets, prepared as described in an upcoming section,

were mounted on a positioner which allowed adjusting the incidence angle, θ_{in}. As shown in Fig. 3.1, the surface was placed at the entrance focus of a 160° spherical sector electrostatic spectrometer, which defined the interaction region from where electrons were emitted with different energies and angles. Electrons emitted from the surface in the forward direction were then deflected into the spectrometer and were analyzed in energy and angle. The spectrometer consisted of a 160° spherical sector analyzer followed by a drift region of approximately 7 cm and a position sensitive detector (PSD) located at the end of the drift space as shown in Fig. 3.1. For a given applied voltage across the sectors of the analyzer electrons with the desired kinetic energy were transmitted through the analyzer, flew through the drift region, and were detected by the PSD. The position of the particle hitting the detector was recorded and lead to the measurement of two orthogonal components, *i.e.* θ_x and θ_y, of the electron polar emission angle θ which will be more precisely defined in chapter 5. Therefore by tuning the spectrometer to a given voltage three electron variables were measured *i.e.* the emission energy E, and the two angles θ_x and θ_y. Finally by scanning the voltage across the sectors of the analyzer a triply differential (energy and two angles) electron emission spectrum could be obtained.

Ions scattered from the surface transited the electron spectrometer and exited via a circular hole (subtending a $\sim 9°$ full angle from the entrance focus) in the outer sector. The exiting ions were limited vertically (in the side view of Fig. 3.1) to an extent of 1 mm prior to charge state analysis, which was provided by electrostatic vertical deflection toward a discrete dynode electron multiplier serving as an ion detector. The overall flight path from the surface to the detector is about 1 m; the detector was offset from the undeflected incident beam axis by $\sim$ 40 mm. In the absence of a field in the charge state deflector, the ions were collected in a shielded and suppressed Faraday cup. The ion detector was mechanically fixed with respect to the faraday cup and both devices could move as a unit only along the y-direction shown in Fig. 3.1. The scattered ions were not limited in the y-direction

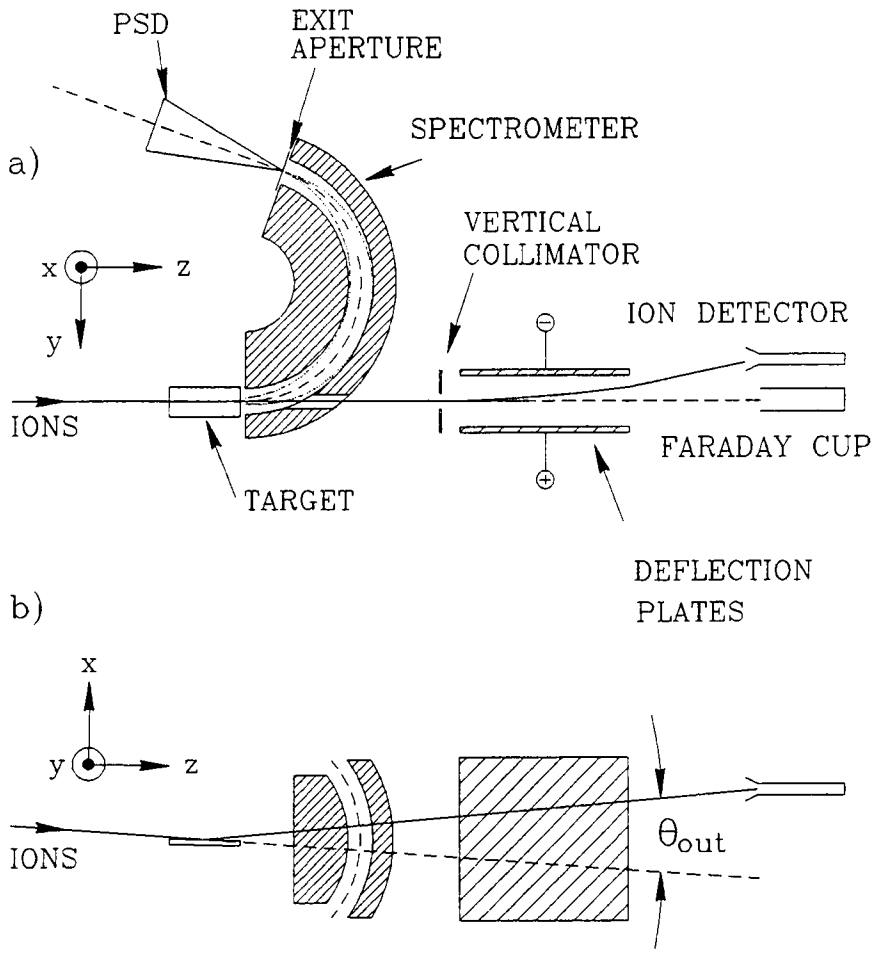

Figure 3.1: Schematic of the apparatus. a) Side view displaying the plane of electrostatic deflection of electrons and ions. b) Bottom view displaying the plane in which the angular distribution of scattered ions was measured.

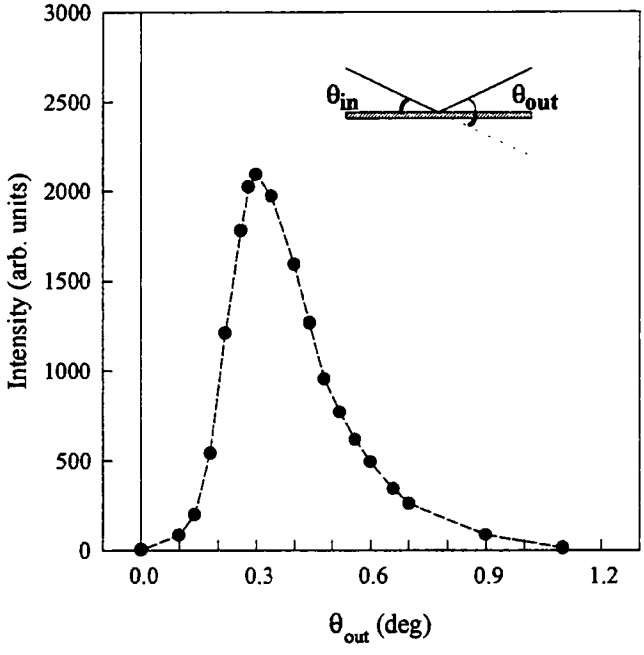

Figure 3.2: Angular distribution of C^{4+} ions scattered from a silicon (100) surface. The spectrum was produced by C^{2+} projectile ions incident at $\theta_{in} = 0.15°$ measured with respect to the surface. The scattering angle θ_{out} was measured with respect to the incident beam direction and is shown in the inset of the figure.

(shown in the bottom view of Fig. 3.1) to permit measurement of their angular distribution by means of measured detector translation in that direction. A 2 mm ion detector entrance aperture subtends a solid angle of 0.15° from the interaction region, which in turn determines the experimental angular resolution of the ion detector. The resolution of the charge state distribution measurements is determined by the combined effect of the size of the aperture and of the slits in front of the charge state analyzer.

Fig. 3.2 shows a typical angular distribution of 3.6 MeV carbon ions with outgoing charge state $q_{out} = 4$ after scattering from silicon(100) at a grazing angle of $\theta_{in} = 0.15°$ with respect to the surface. A schematics of the ion scattering geometry

displaying the angles θ_{in} and θ_{out} is shown in the inset of Fig. 3.2. The outgoing scattering angle, θ_{out}, was measured with respect to the incident beam direction. The straight line at $\theta_{out} = 0°$ indicates the position where unscattered C^{4+} ions would be detected in the absence of the surface. The distribution was peaked near $\theta_{out} = 2\theta_{in} = 0.3°$, showing that the ions were specularly reflected. The measurements did not fully vanish for $\theta_{out} < \theta_{in}$ because of the large acceptance angle of the ion detector.

In order to obtain outgoing charge state distributions, the detector position was fixed at the peak of the angular distribution shown in Fig.3.2 and the electric field between the deflection plates was scanned in order to sequentially deflect and measure the intensity of each charge state present in the scattered beam into the ion detector. Since the acceptance angle of 0.15° was smaller than the width of the angular distribution of 0.4°, only a fraction of the scattered ions were measured. Fig. 3.3 shows typical charge state distributions obtained for two different projectile kinetic energies. The main exit charge state components were $q_{out} = 3, 4$ at the lower collision energy and $q_{out} = 4, 5$ at the higher energy.

Coincidence measurements were performed between an electron emitted in the ion-surface collision and an ion specularly reflected from a silicon(100) surface. The coincidence setup permitted measuring the energy and angular distribution of emitted electrons detected in coincidence with an outgoing ion scattered at a given scattering angle θ_{out}, and in a particular charge state q_{out}. The advantages of using this technique were two fold: i) Electrons produced in processes other than the ion-surface interaction were not counted in the electron coincident spectrum. ii) Absolute measurements of electron emission spectra were performed from which a yield could be extracted.

In the following paragraphs the apparatus will be described in more detail.

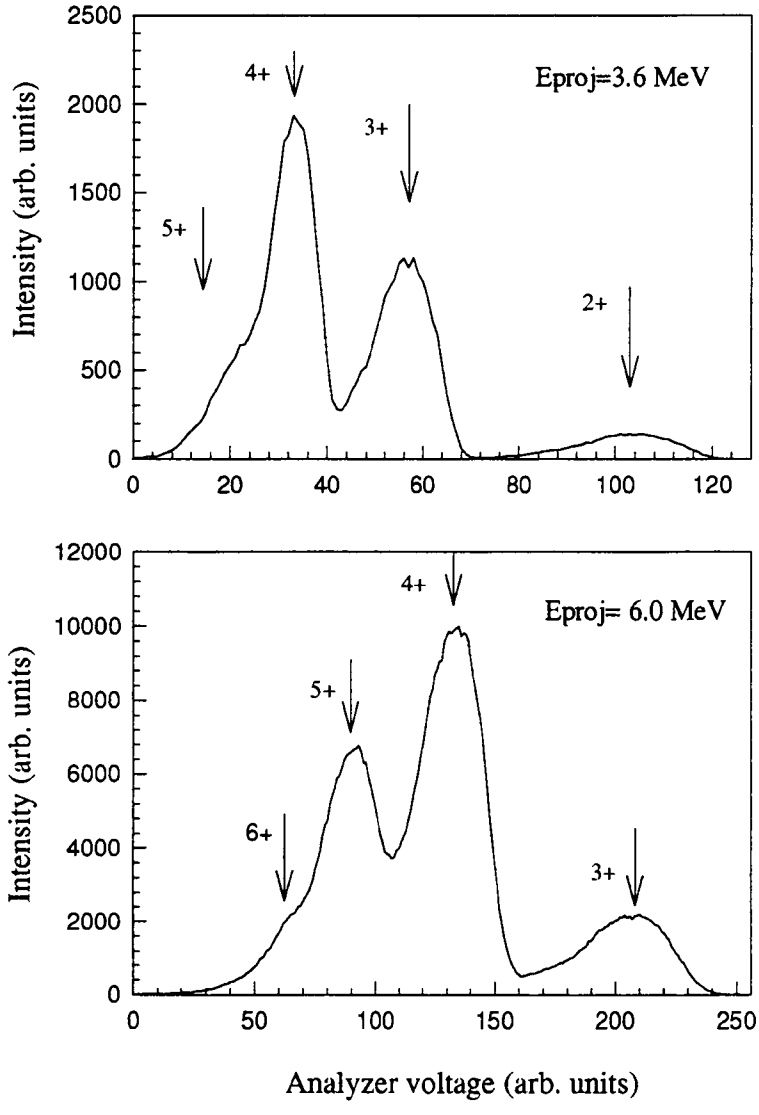

Figure 3.3: Outgoing charge state distributions produced by various $C^{q_{in}+}$ ions scattered by a silicon surface at total kinetic energies of 3.6 MeV (top), and 6.0 MeV (bottom).

3.2 UHV chamber

The ultrahigh vacuum chamber was pumped by two turbomolecular pumps connected in series and by a cryopump. The base pressure in the chamber was 8×10^{-11} Torr. This pressure was achieved after baking the chamber for 2 days at an average temperature of 150° C. The power supply that feeds current to the heating tapes as well as the temperature measurement of the chamber made by using type K (Cromel- Alumel from Cole-Palmer) thermocouples attached to the outside chamber walls were controlled remotely by a computer; this allowed leaving the chamber unattended while being baked. A residual gas analyzer (RGA) connected to the chamber was used to monitor the presence of different chemical elements in the chamber during the baking cycle. The main components in the chamber before baking were nitrogen and water. After the baking cycles the levels of water and nitrogen decreased and the residual gas in the chamber was mostly hydrogen. The pressure in the UHV chamber following this method was typically in the high 10^{-11} Torr range. Pressures of this kind are necessary to provide the clean environment required to study the interaction of ions with surfaces as will be discussed in Section 3.4.

3.3 Sample holder and calibration of the incident angle

Fig. 3.4 shows the sample holder which consists mainly of two rectangular strips of tantalum serving as supports upon which the target lies. The surface is fixed by two tantalum clamps which are spotwelded to the tantalum supports. The tantalum supports are isolated electrically from a stainless steel base by alumina spacers. Each tantalum strip has two electrical connections making a total of four. To heat the surface one pair is used to run current through the crystal bulk while the other pair is used to measure the voltage drop across the surface. In addition by connecting a picoammeter to either of these electrical connections during beamtime, the fraction of beam current intercepted by the crystal can be measured.

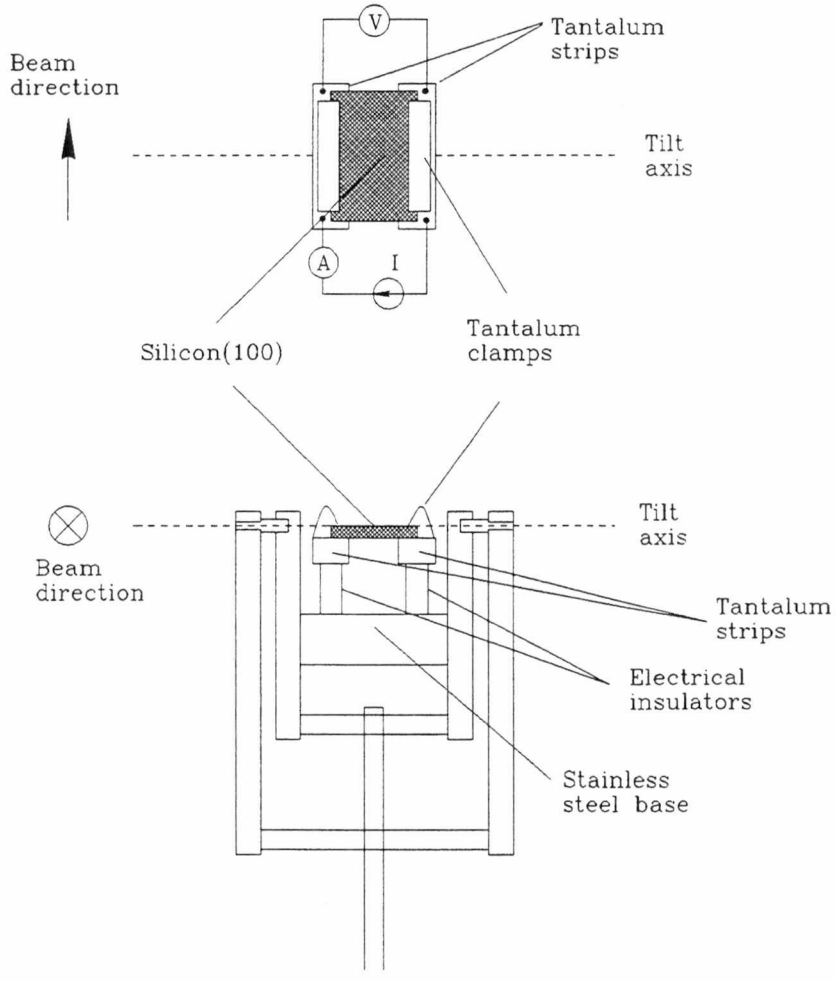

Figure 3.4: Schematic diagram of the sample holder

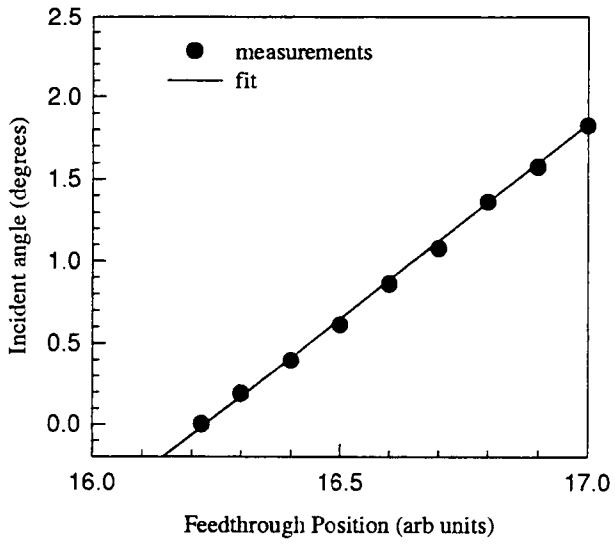

Figure 3.5: Calibration of the incidence angle θ_{in} vs. the feedthrough position. The calibration was obtained by directing a laser beam onto the surface. See text for details.

The stainless steel base shown in Fig. 3.4 serves as a frame for the sample holder. The frame and therefore the surface can be tilted within a 10° range about a "tilting" axis as shown in the figure. The tilt of the sample determines the angle of incidence θ_{in} of the incoming ions with respect to the silicon surface. The tilt angle, and therefore the angle of incidence, is adjusted by a rotation-to-linear motion feedthrough in the following way: A micrometer barrel is rotated manually at the feedthrough resulting in the translation of a linear rod that connects to the sample holder. This translation of the rod then leads to a tilt of the sample about the tilting axis shown in Fig. 3.4. The tilt of the sample (*i.e.* the angle of incidence θ_{in}) then needs to be calibrated against the rotary-to-linear-motion feedthrough position.

A calibration as shown in Fig. 3.5, of the incident angle θ_{in} against the micrometer reading on the rotational-to-linear motion feedthrough, is made employing a laser. A laser beam is directed towards the silicon surface. The angle θ_R of the

reflected beam measured with respect to the surface normal is then recorded for different feedthrough positions leading to different tilt angles. The angle of incidence θ_{in} is related to θ_R by

$$\theta_{in} = \frac{\pi}{2} - \theta_R. \tag{13}$$

Initially the surface is aligned perpendicular to the incident beam (*i.e.* $\theta_R = 0$) which defines the zero degree position $\theta_{in} = 0$. Keeping the laser beam direction fixed, θ_R is then recorded for several feedthrough positions. Using equation 13, θ_{in} is calibrated and plotted vs. feedthrough position as shown in Fig. 3.5. This provides the calibration of the angle of incidence θ_{in} against the dummy rotary-to-linear motion feedthrough reading. As observed in the figure there is a a linear relation between the incident angle and the feedthrough position over the range of angles utilized in the experiment, providing a direct way of adjusting θ_{in}.

The feedthrough position equal to 16.20 corresponds to an angle of incidence of zero degree as indicated by the calibration using the laser. In addition to this method a fine determination of the zero degree position ($\theta_{in} = 0$) is performed during beamtime by measuring the beam current intercepted by the surface for various angles of incidence as shown in Fig. 3.6. A minimum in the graph of intercepted target cur rent versus incidence angle feedthrough position is reproducibly observed to separate a region of large slope from one of low slope. For larger values the beam current rises rapidly as a result of large secondary electron emission and increasing probability of ions penetrating the surface. At the minimum the average beam trajectory is parallel to the surface. For smaller position values the current intercepted by the surface increase slightly because of interception of beam particles by the leading target edge. The minimum value is reproducible with a precision better than 0.05° and matches the value determined as zero angle of incidence, $\theta_{in} = 0$, obtained using the laser calibration. In this way the zero degree position could be determined easily during beamtime for different experimental runs.

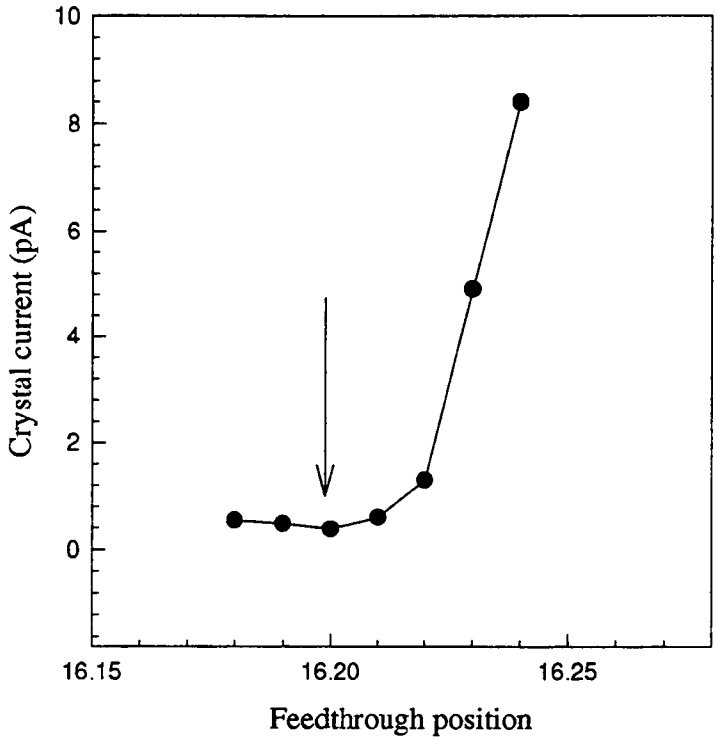

Figure 3.6: Determination of the zero degree feedthrough position.

3.4 Surface preparation

To perform the experiments the surfaces must be flat and clean. Single-crystal silicon targets were obtained from 0.5 mm thick silicon wafers which were manufactured so that the angle between the surface plane and the (100) crystal plane was 0.4° as indicated by x-ray diffraction measurements performed by Texas Instruments [34]. This inclination leads to terrace steps spaced by approximately 20 nm on average. Using additional information from the manufacturer it was possible to mount the final target crystals so that the ion beams passed parallel to the average terrace edges. Assuming an orientation precision better than 5°, the distance between adjacent terrace edges encountered by the ions exceeded 200 nm on the average. Rectangular samples of about 18×9 mm^2 were cut from the wafers and mounted on the sample holder. The shape of the angular distribution of scattered ions provided information that helped to characterize the surface flatness as will be discussed in the next

chapter.

To remove the initial silicon-oxide layers and to anneal the surfaces, the targets were heated by passing a current through the bulk crystal following a prescription developed by Swartzentruber *et al.* [35]. The process consists in outgassing the surface for a few hours at a temperature below 900°C pressure in the chamber in the 10^{-10} Torr range (the period of time is determined by how long it takes for the pressure in the chamber to return to its initial value after the outgassing cycle is started). Once this was achieved the temperature was increased close to 1200°C for 2 minutes to remove the oxide layer by sublimation. After the 2 minute flash heating, the temperature was brought rapidly to 900° C and from there was decreased slowly at a rate of 2°C/sec to room temperature. The temperature of the surface was monitored by using an optical pyrometer.

After heating the target a clean surface is obtained although this doesn't last forever. After time the surface can be covered with contaminants from the residual gas inside the chamber (even at 10^{-10} Torr). A simple expression can be derived from kinetic gas theory which estimates the time ,τ, that it would take to build up a monolayer of atoms on top of a clean surface [36] and is given by

$$\tau = \frac{10^{-6}}{s.p} \tag{14}$$

where τ is the time in seconds, s is called the sticking coefficient and p the pressure expressed in mbar inside the chamber. According to this expression, assuming s=1 and $p = 10^{-10}$ mbar, it would take about 2.7 hours to build a monolayer. This implies on one hand that UHV conditions or better are essential to work with clean surfaces. However in reality the sticking coefficient may be smaller than one depending on the surface utilized and the temperature of the surface.

The evolution of the electron spectra with time is seen not to cause significant changes in the overall shape over periods larger than 24 hours. This hasn't been systematically investigated since over such periods of time in a typical beam time

(maximum of seven days) the collision conditions are changed. A study of such systematics would require an entire beam time leaving the collision conditions fixed (projectile type, velocity and charge state). However few observations performed under fixed collision conditions over periods above 24 hours show only a slight increase of the convoy to binary intensity ratio of less than 5%. This seems to indicate that equation 14 only provides an upper limit for the time of monolayer coverage. In reality, the silicon surfaces used seem to offer a larger time frame in which to work, suggesting that silicon may have a sticking coefficient $s < 1$ and therefore being more inert to adsorb particles on the surface. Because of this reason the surface is flashed to 1200°C only once at the beginning of a typical beamtime (7 days). All other heating treatments to the surface only involve outgassing cycles below 900°C which is repeated approximately every 24 hours since the first flashing procedure.

3.5 Electron detection

The electron spectrometer consists of a 160° spherical sector analyzer plus a position sensitive detector which permits analyzing the energy E and two orthogonal components of the polar emission angle θ of the emitted electrons. The analyzer as shown in Fig. 3.1 consists of two concentric spherical sectors to which a potential difference is applied. The resulting electric field between the sectors is $\propto 1/r^2$, where r is the radial position with respect to the sectors common center.

This analyzer preserves to a good degree the focal properties of the 180° spherical analyzer, described in detail by Sevier [37], and gives us the additional advantage of removing the entrance focal point from the sector boundaries making it possible to place the target at the entrance focus of the analyzer (which is physically impossible in the case of the 180° analyzer). The 180° analyzer is double focusing since it can focus trajectories corresponding to a common object point to a common image point in two planes, one being the plane in which the electrons are deflected, referred to as the *deflection plane* and the other being the plane perpendicular to the deflection

plane, referred to as the *perpendicular plane.* In the perpendicular plane the focusing is perfect (two trajectories originating at the same object point, launched with two different angles and entering the analyzer with exactly the same energy will fall on the same image point). However in the deflection plane the image point is focused to first order in the emission angle (a trajectory launched with an angle α with respect to the central ray trajectory will fall a distance $x \propto \alpha^2$ from the image point. First order corresponds to being $\frac{\partial x}{\partial \alpha} = 0$ in a Taylor expansion of x vs. α.).

The presence of stray magnetic fields affect the focusing properties of the analyzer. To reduce this effect in our apparatus, the inside walls of the UHV chamber were covered with a thin sheet of a high magnetic permeability material [38] reducing the effect of residual magnetic fields in the interior of the chamber to less than 10 mgauss.

Electrons emitted with different energies will follow different trajectories. By means of an aperture located at the exit focus of the analyzer only electrons with the desired energy E_o may be selected by adjusting the voltage across the sectors $\Delta V \equiv V_{out} - V_{in}$. The applied voltage is related to the desired electron energy E_o by the analyzer constant C [37] as

$$\Delta V = C E_o. \tag{15}$$

C can be obtained from geometrical parameters ([37] p.21) as

$$C = \frac{r_{out}}{r_{in}} - \frac{r_{in}}{r_{out}}, \tag{16}$$

where r_{in} and r_{out} correspond to the inner and outer radii of the sectors. For our analyzer the analyzer constant used was $C = 0.454$. Due to the finite width w_2 of the exit aperture, electrons with energies in an interval δE (energy pass band of the spectrometer) about E_0 will still be transmitted through the analyzer and impact the detector (as opposed to the case of an ideal spectrometer in which $\delta E = 0$).

The energy pass band δE of an analyzer can be defined as the full width at half maximum of the transmission function T(E) of the spectrometer which measures the probability of an electron with energy E being transmitted through the analyzer. As explained in ref. [37] T(E) can be approximately described by a trapezoidal function with base width δE_{base}, full width at half maximum δE_{fwhm} and top width δE_{top} expressed in terms of geometrical parameters as:

$$\begin{aligned} \delta E_{top} &= \frac{(w_1 - w_2)}{2\bar{r}} E_o \\ \delta E_{fwhm} &= \frac{max(w_1, w_2)}{2\bar{r}} E_o \\ \delta E_{base} &= \frac{(w_1 + w_2)}{2\bar{r}} E_o \end{aligned} \tag{17}$$

were w_1 and w_2 represent the sizes of the entrance and exit apertures and $\bar{r}$ is the mean radius of curvature of the analyzer *i.e.* $\bar{r} = \frac{r_1+r_2}{2}$. For our case $\bar{r} = 5.47$ cm and $w_2 = 1$ mm and is larger than the entrance aperture defined by the beam diameter which is $w_1 = 0.2$ mm. The spectrometer energy resolution is defined by the ratio of $\delta E/E$. Normally either the base width δE_{base} or the full width at half maximum δE_{fwhm}, of the transmission function, can be used in defining the energy resolution. Choosing then $\delta E_{fwhm}/E$, the calculated resolution is 0.91%. Experimentally an upper limit value for the energy resolution could be obtained from the electron spectrum, shown in Fig. 3.7, produced by electrons impinging on a silicon surface. Electrons produced by an electron gun (Perkin Elmer) were incident at $\theta_{in} = 45°$ with respect to the surface resulting in the emission of electrons with energies between 0 to about 930 eV. The spectrometer was positioned at approximately the specular beam direction i.e. at $\theta_{out} = 90°$ with respect to the beam direction (the convention for θ_{in} and θ_{out} is shown in the inset of Fig. 3.2). A peak at 920 eV is observed corresponding to electrons elastically scattered from the surface. The width of the peak results from mainly three contributions: The width of the energy distribution of the primary electron beam (estimated from the manufacturer's literature to be

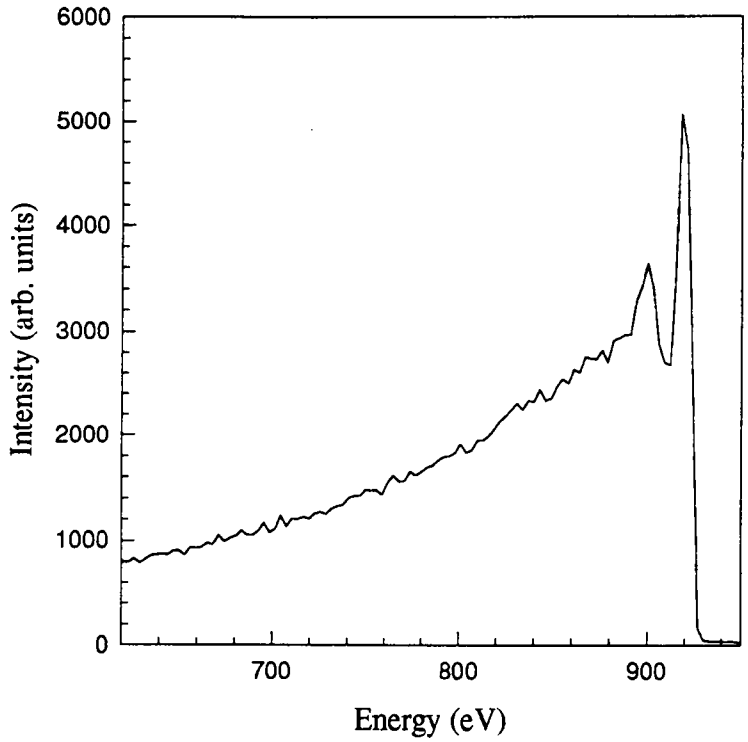

Figure 3.7: Energy distribution of emitted electrons produced by electrons impinging on a silicon(100) surface at an incident angle of $\theta_{in} = 45°$. The peak observed at 920 eV corresponds to electrons elastically scattered from the surface.

$\leq$ 1 eV), the broadening of this primary distribution due to the scattering process (energy loss and straggling) and the spectrometer resolution. Assuming that the broadening of the peak is purely due to the spectrometer resolution the FWHM of the peak provides an upper limit for the spectrometer energy resolution (i.e. the resolution should still be better than this measured value). As observed in the spectrum FWHM/Epeak $\sim$ 0.011 which means a 1.1% energy resolution for electrons of 920 eV.

Electrons exiting the spectrometer transit a drift region of 7 cm before being detected by a position sensitive detector (PSD) shown in Fig. 3.8. When the ion beam enters the chamber a considerable amount of low energy electrons arising from different sources can be produced and eventually reach the detector leading to a large

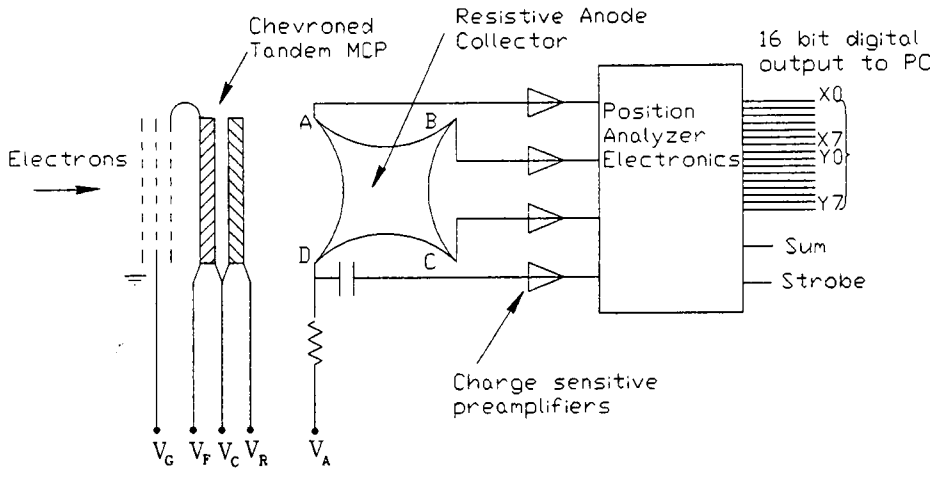

$$\frac{x}{a} = \frac{Q_B + Q_C}{Q_A + Q_B + Q_C + Q_D}$$

$$\frac{y}{a} = \frac{Q_A + Q_B}{Q_A + Q_B + Q_C + Q_D}$$

Figure 3.8: Schematic diagram of the position sensitive detector. In front of the detector there is a set of three grids used to retard low energy electrons and to accelerate the electrons transmitted through the grids towards the front plate. Also shown is the algorithm performed by the position decoder unit to determine the position information.

background contribution. Just to mention an example ions scattered at the slits could produce electrons, which when hitting the walls of the chamber, will liberate a large amount of low energy electrons. This contribution to the background is suppressed by shielding the drift region and in addition by retarding electrons with energies below $E = 20$ eV by biasing accordingly a set of 3 grids located in front of the PSD shown in Fig. 3.8. As shown in the figure the first grid is connected to the GND potential of the chamber. The second grid is biased at $V_G = -20$ V which repels the low energy electrons. Finally the third grid is connected to the front plate potential, V_F of the PSD which is biased typically at $V_F = 200$ V to accelerate the detected electrons towards the PSD to an energy regime where the detection efficiency of the microchannel plates is higher.

The effective angular resolution of the electron spectrometer is determined in principle by the detector resolution, the electronics resolution and a contribution due to the finite source size and the extent of the exit aperture. From these three factors the last one dominates. Trajectories passing through the exit aperture with angles within an interval $\delta\theta$ will fall on the same spot on the detector. The interval $\delta\theta$ determines the angular resolution and is given by

$$\delta\theta = \arctan \frac{w_2}{D}, \tag{18}$$

where D is the distance between the exit aperture and the electron detector. For our case $w_2 = 1$ mm, $D = 7$ cm and therefore $\delta\theta = 0.82°$. Both estimates of $\delta E/E$ and $\delta\theta$ are probably optimistic since they assume the electrons to be emitted from a point source. In reality the source size is defined by a region on the surface intercepted by the ion beam which corresponds to an extended source.

3.5.1 Position sensitive detector

As mentioned in the above section a PSD is used to detect the electrons. The detector consists of a pair of microchannel plates (MCP) and a resistive anode. An electron

hitting on the front channel plate produces a charge pulse of $\sim 10^6$ electrons exiting the rear plate when a voltage of about 900 V is applied across each of the plates (i.e. $V_F - V_C = V_C - V_R = 900$ V in Fig. 3.8). The charge pulse exiting the rear plate is accelerated by about 300 V on to the resistive anode where a total of four signals are generated from the four corners which are used ultimately to determine the position at which the charged particle struck the detector. The voltages to bias the MCP as well as the resistive anode are provided by using a combination of two power supplies and a voltage divider.

The four signals from the resistive anode are preamplified and analyzed by a position analyzer electronics unit (position decoder) that generates a 16 bit digital position information output corresponding 8 bits each for the x and y coordinates respectively. In addition, SUM and STROBE output signals are available from the Position decoder. The SUM signal is a bipolar analog pulse which is obtained by summing the four preamplified output pulses of the resistive anode. The STROBE pulse is generated after the digitized position signal becomes available which happens at about 20 us after the initial event occurs.

3.6 Coincidence Electronics setup

A schematic diagram of the coincidence setup is shown in Fig. 3.9. A brief overview of the setup operation is as follows. The electron spectrum is acquired by a custom made [39] data acquisition system composed mainly of an IBM PC compatible computer, that runs a software program which allows reading, storing and displaying the data, and two NIM modules (PSD and DOSE interface modules) which serve as interface between the electron and normalization signals and the PC. The PSD interface module has a gate input which controls whether an event must be acquired or not. In our case this gate is fed by the output of a time to amplitude converter (TAC) which indicates when an electron has been detected in coincidence with an ion scattered in a given exit charge state and exiting angle. In the following paragraphs

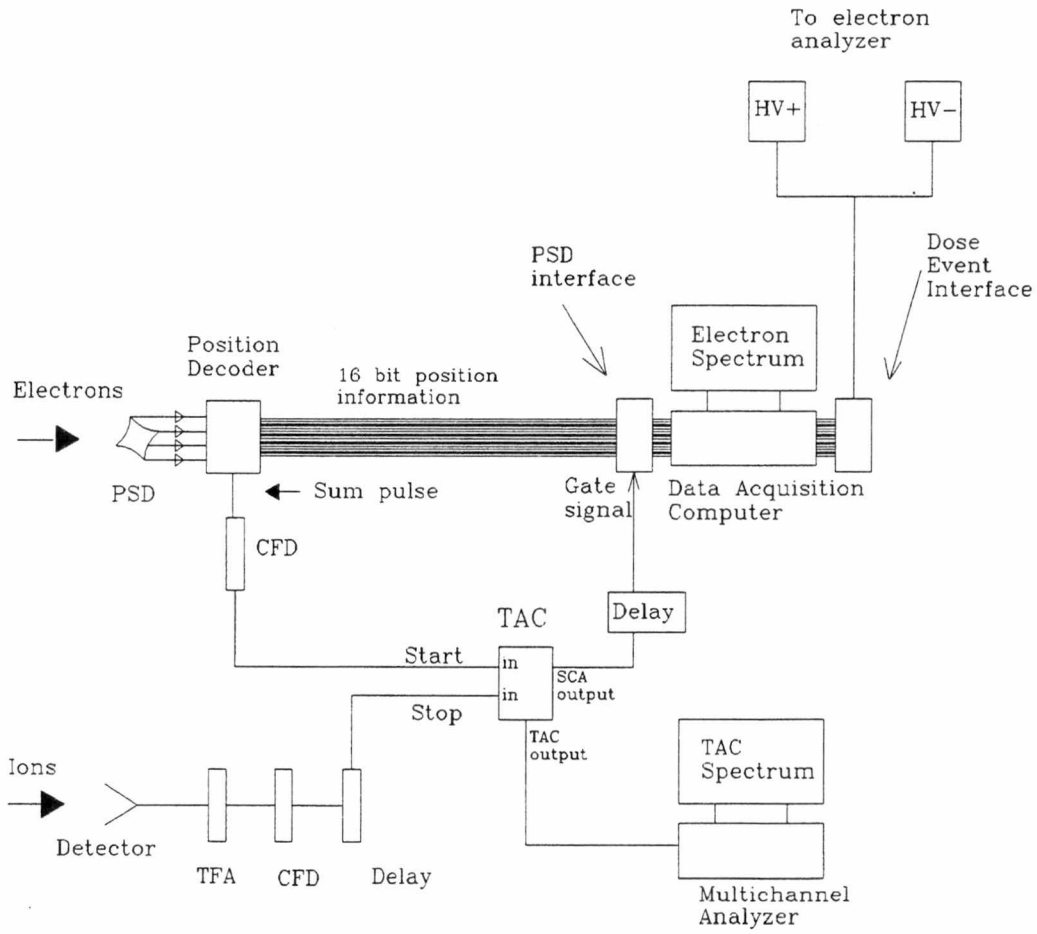

Figure 3.9: Schematic diagram of the coincidence electronics setup

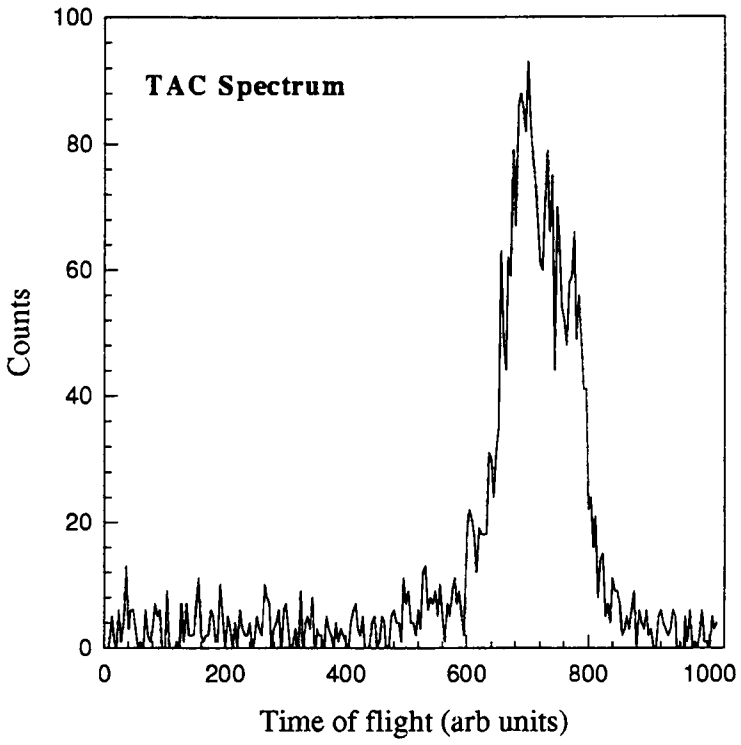

Figure 3.10: TAC spectrum produced by 6.0 MeV carbon ions incident at 0.15° upon a silicon (100) surface.

a more detailed explanation of the detection system will be described.

The heart of the coincidence setup is a time to amplitude converter (TAC). In the experiment the start signal was generated by the detection of an electron while the stop signal was produced by the detection of an outgoing ion. The pulses generated by the TAC are sent to a multichannel analyzer (MCA) which accumulates the events in different channels according to the pulse amplitude. Since the amplitude of the logic pulse generated by the TAC is proportional to the time difference between the start and stop inputs, the horizontal axis of the TAC spectrum as shown in Fig. 3.10 represents the time of flight of the ion to the ion detector. The most probable times of flight indicated by the position of the peaks in the TAC spectrum are 120 ns and 90 ns for 3.6 MeV and 6.0 MeV projectiles respectively. The events in the peak indicate coincidences between the detected electron and exiting ion, while the background

represents random coincidences resulting from detection of an ion which did not produce the detected start electron but did still stop the TAC. This background results from high beam particle currents and can be minimized by using low beam currents. As shown in the figure, typical signal to background ratios were about 10. The width of the peak, typically about 30 ns, is determined mainly by the quality of the timing signals used as start and stop rather than by the velocity distribution of the electrons and the exiting ions. After the TAC spectrum is acquired, only events in the peak can be selected by setting discriminator levels in the TAC. The discriminated output is sent to gate the PSD interface. The peak is composed of coincidence and background events. The number of background events is estimated assuming a constant value determined by measuring the intensity of the constant background outside the peak. This information is used to estimate the number of background events within the peak which is subtracted off the total number of events inside the peak. The resulting number corresponds then to the coincidence events.

Fig. 3.11 shows a timing diagram of the most relevant signals used in setting the coincidence electronics. The SUM signal from the position decoder box, introduced in section 3.5.1, is used as the timing signal for the electrons and is fed into a CFD which later generates a fast negative NIM output pulse used as the start of the TAC. The pulse produced by the electron multiplier is used as a timing signal for the ions which, after being amplified and delayed, is sent to a CFD whose output is used as a STOP input to the TAC. A TAC/SCA output pulse is generated for an event occurring within the peak of the TAC spectrum. This output signal is used to gate the PSD interface module so only coincident electrons present at the input of the PSD interface module will be read by the data acquisition computer.

3.6.1 Data Acquisition

The data acquisition system consists mainly of a IBM-PC compatible computer running a software program named SIDA designed to acquire, display and store the

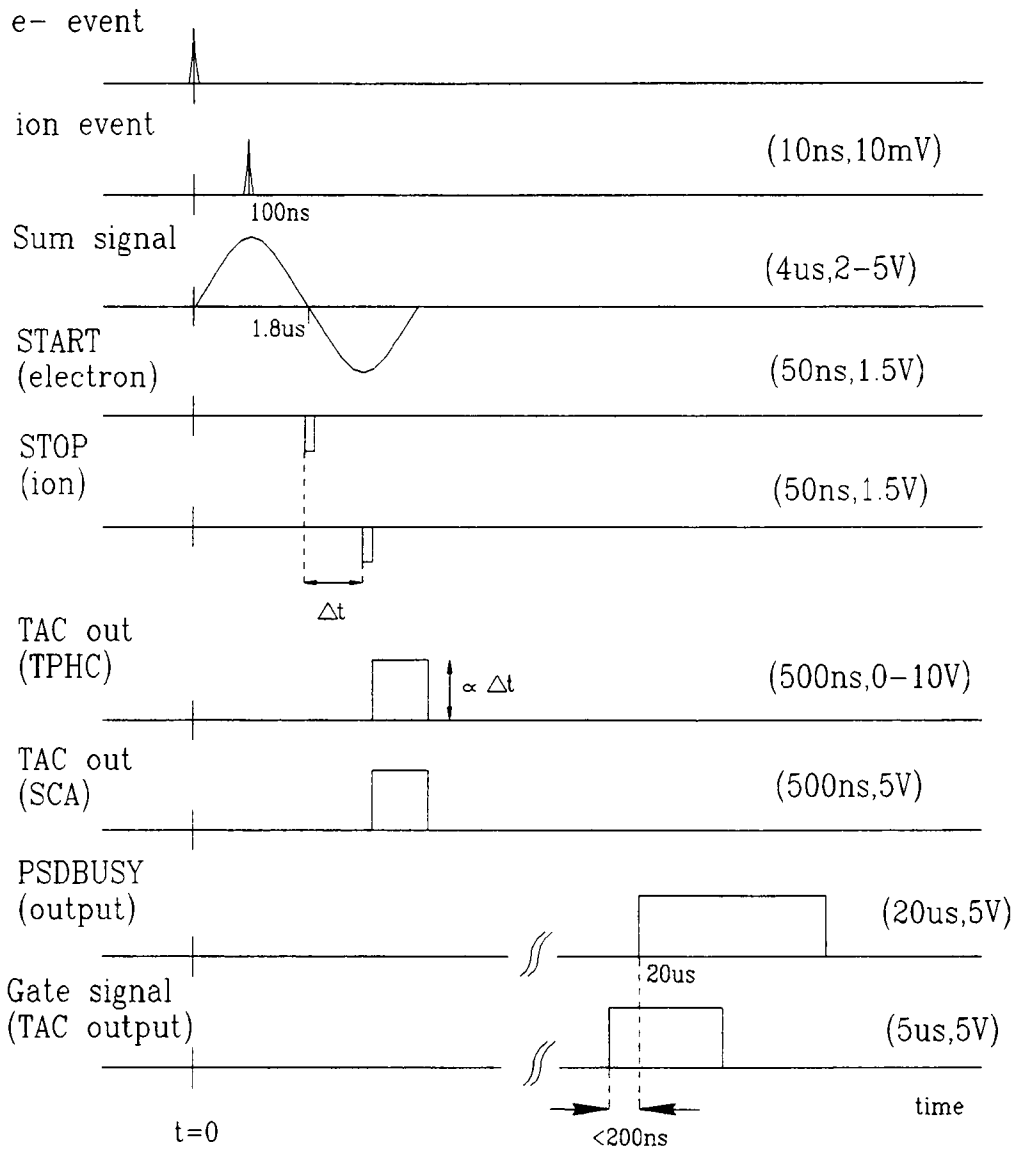

Figure 3.11: Timing Diagram corresponding to the coincidence electronics setup. The pair of numbers (t,V) displayed on the right hand side indicate the time width and amplitude of the pulses.

data in addition to two interface NIM modules (PSD and DAC/DOSE interface modules) that in turn interface with two Metrabyte model PI012 interface cards installed in the computer. There are two main tasks performed by the program in our experiment. One is to send a 12-bit number to a DAC which controls the programmable power supplies that supply the voltage to the sectors of the electron analyzer which in turn selects the energy, E, of the electrons being detected. This is done through the DAC/DOSE interface module. The other main task is to count the number of electrons detected as well as to read the 16-bit digital (x, y) position information of an electron hitting the detector, which is done via the PSD interface module.

A PSD event (electrons) is stored in a 3D array and characterized by 3 indices (x, y, E) where x and y represent the horizontal and vertical position coordinates of an electron hitting the detector and E the electron energy. In order to store the information in the available memory the precision of these quantities was reduced to 6 bits (64 channels) for x, 3 bits (8 channels) for y and to 7 bits (128 channels) for the electron energy E.

The signal (ions) from the electron multiplier detector is sent to a single channel input of the DOSE interface module for normalization. In this way the voltage on the spectrometer will be incremented after a predetermined amount of projectiles are collected in the ion detector

A PSDBUSY output signal on the PSD interface module indicates when the input bits corresponding to the x and y position information were latched. This signal is used to adjust the timing of the TACSCA output signal from the TAC which corresponds to the gate signal (shown in Fig. 3.9). The timing of the gate signal is adjusted in the following way: For a 16-bit position information event at the input port of the data acquisition system (*i.e.* located at the entrance of the PSD interface module to be read by the computer, (see Fig. 3.9) the gate signal (*i.e.* the TACSCA output from the TAC) must be present and stable before the event

position information is latched (Locate on Fig. 3.9 the gate signal the 16-bit position information and the PSDBUSY output on the PSD interface). The correct timing of these two signals (*i.e.* the gate and the PSDBUSY output signals) is shown in Fig. 3.11. Once the timing is adjusted the gate signal is fed into the PSD interface module.

4 Scattering of Ions

4.1 Overview

As discussed in the experimental setup section, measurements of the angular and charge state distribution of projectile ions scattered from the silicon(100) surface were made. Carbon ions with initial charge states $q_{in} = 1$ to $q_{in} = 3$ and with total kinetic energies between 2.4 MeV and 6.0 MeV were used. Angular distributions measured for different projectile energies and incident angles indicate that, at the projectile velocities utilized, the ions scattered from the silicon surface follow a trajectory corresponding to the case of specular reflection. Measurements of the charge state distributions for carbon ions scattered from the silicon (100) surface as well as for ions transmitted through a thin carbon foil were also made. The ions interacting at grazing incidence with the silicon surface achieve charge state equilibration for the projectile velocity regime studied. In addition differences between the charge state fractions measured under grazing incidence with a silicon surface and under normal incidence with a carbon foil target are discussed.

4.2 Angular distributions of scattered ions

A typical angular distribution of carbon ions scattered from the silicon (100) surface is shown in Fig. 3.2. Similarly Fig. 4.1 shows an angular distribution for a carbon projectile incident at a slightly larger incident angle of 0.23° and impact energy of 6.0 MeV. As in the former case the distribution is asymmetric, having a steeply rising slope for the small scattering angles and a slowly decreasing slope for the larger angles. The distribution peaks at about $\theta_{out} = 0.45°$ indicating ions scattering from the Si(100) surface in the specular direction . The signal does not vanish completely for $\theta_{out} \sim \theta_{in}$ (where supposedly the emission is obscured by the surface) due to the large acceptance angle of the ion detector. The steeply rising slope of the distribution

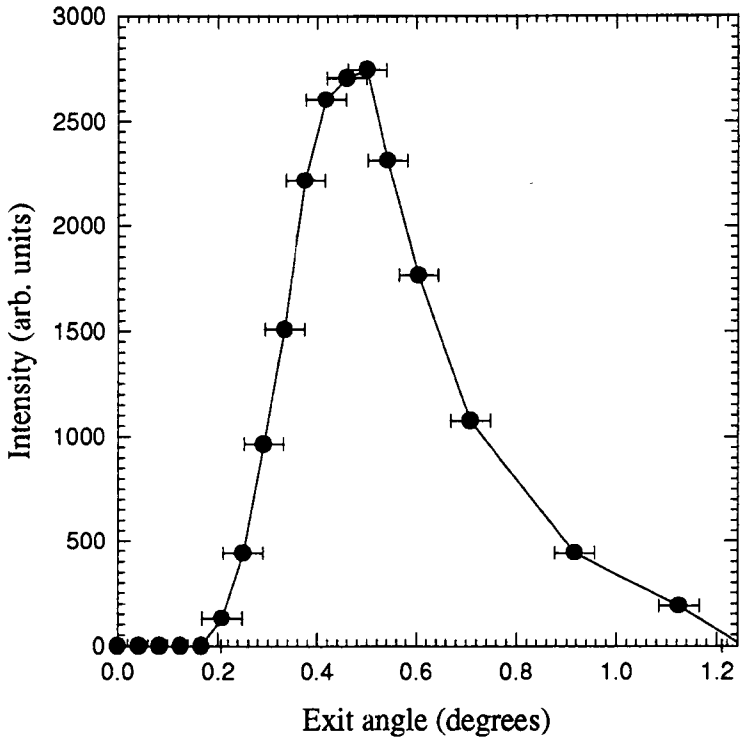

Figure 4.1: Angular distribution of C^{4+} ions scattered from a silicon (100) surface. The spectrum was produced by 6.0 MeV C^{3+} projectile ions incident at $\theta_{in} = 0.15°$.

for small angles is consistent with what would be expected for ions scattered from a flat surface. For particles scattering from a rough surface instead, the projectile ion would encounter bulk type interactions resulting in a large number of events in the region of $\theta_{out} < 2\theta_{in}$ and therefore a larger width which is not observed in our measurements.

The asymmetric tail at higher angles arises from multiple scattering of the ion with the surface atoms. In addition trajectories that penetrate the surface also can contribute to the tail of the peak due to scattering of the ions with target atoms involving small impact parameters, resulting in large scattering angles. This is seen in the angular distribution as a larger number of scattering events in the region of large θ_{out}. The small size of the tail suggests that the contribution arising from

penetrating trajectories may be small.

In order to further explore the trajectories followed by the ions at these projectile velocities, angular distributions were measured for various incident angles for carbon ions at three different projectile velocities. Fig. 4.2 shows distributions obtained at 3.0 and 6.0 MeV. The width of the distribution increases for larger incident angles, which is consistent, in the context of the above paragraph, with a larger amount of multiple scattering events associated with penetrating trajectories. The position of the peaks have been determined and plotted against the incident angle for three projectile velocities as shown in Fig. 4.3. The data points fall on a straight line which is consistent with specular reflection (within the experimental error of determining the incident and exit angles as indicated by the error bars in the figure). However, a slight deviation towards larger scattering angles is systematically observed for the three projectile velocities at small angles of incidence, $\theta_{out} \sim 0.1°$. The deviation is small and still within the experimental error.

The small deviation from specular deflection for small angles of incidence could be expected if the following arguments are considered: An ion interacting with a surface without changing charge along the trajectory scatters in the specular direction. If the ion changes charge a deviation from the specular direction could occur as the result of competition between the repulsive force exerted by the planar average potential and an the attractive force that results from the DIP. For the collision system studied, the exit charge, $q_{out} = 4$, is larger than the incoming charge state, $q_{in} = 1, 2, 3$; therefore a deviation from specular reflection as seen in the figure could result, according to the above argument, from the interaction between the long range interaction provided by the surface atoms and the projectile ion.

To explore this further, Fig. 4.4 shows angular distributions of exiting 3.0 MeV $C^{q_{out}+}$ with $q_{out} = 1, 2, 3$ scattered from a silicon (100) surface. In all three cases C^{1+} projectile ions were incident at 0.16° . No significant exit charge state dependence is observed, which means that any effect due to image interactions with the scattered

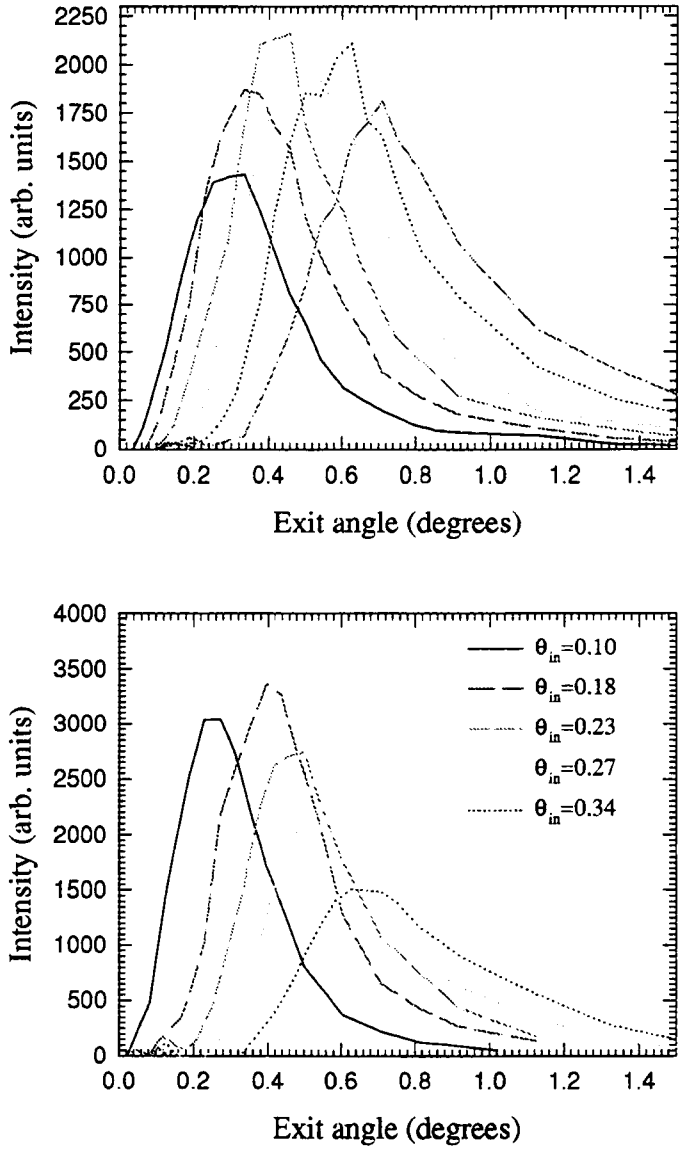

Figure 4.2: Angular distributions for various incident angles for two projectile velocities: a)3.0 MeV b) 6.0 MeV

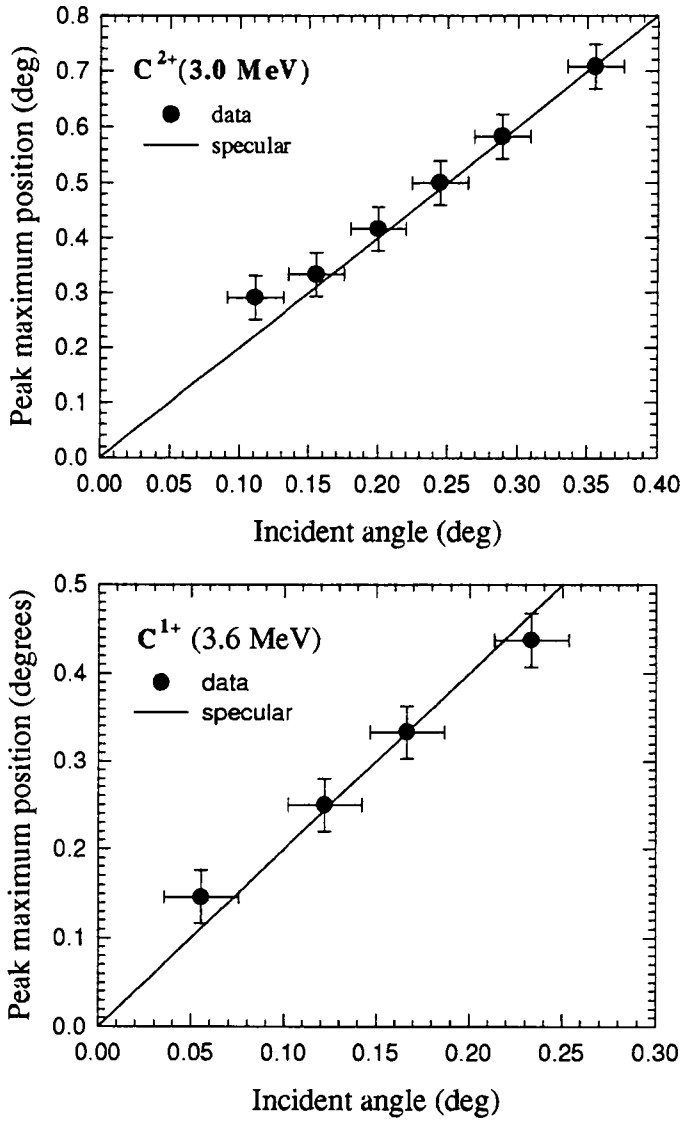

Figure 4.3: Peak maximum position vs. incident angle

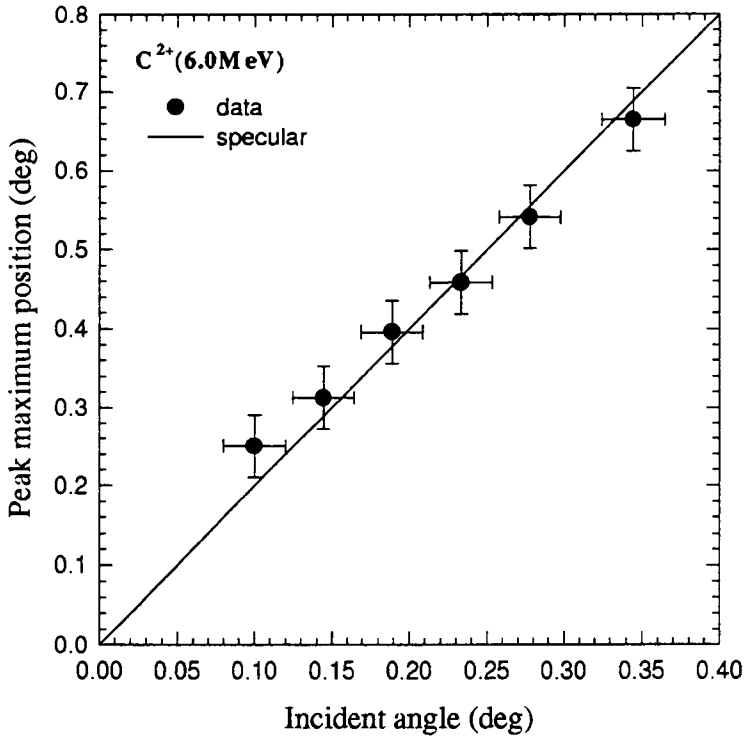

Figure 4.3: (continued)

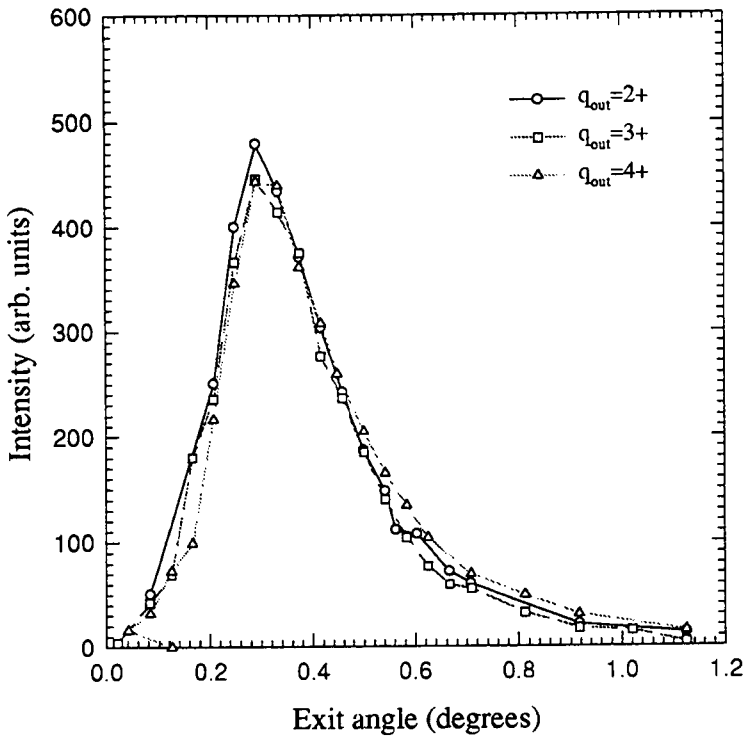

Figure 4.4: Angular distributions of carbon ions scattered in different exiting charge states.

ion after it has changed charge close to the surface must be small and likely to be observed only for smaller incident angles. Such observations, corresponding to angles smaller than $\theta_{in} = 0.1°$, are beyond the precision of the present ion detection.

An interesting result can be observed by determining the FWHM of the peaks from Fig. 4.2 and plotting those widths versus the angle of incidence as shown in Fig. 4.5, where the data points have been connected to guide the eye. For the three impact energies the FWHM increases with the angle of incidence. The main feature to notice is the general shape of each curve rather than the absolute value of each data point. Fig. 4.5 suggests that for each projectile velocity there is a critical value of incident angle, θ'_{crit}, above which the FWHM starts increasing; below this critical value the FWHM appears to be constant.

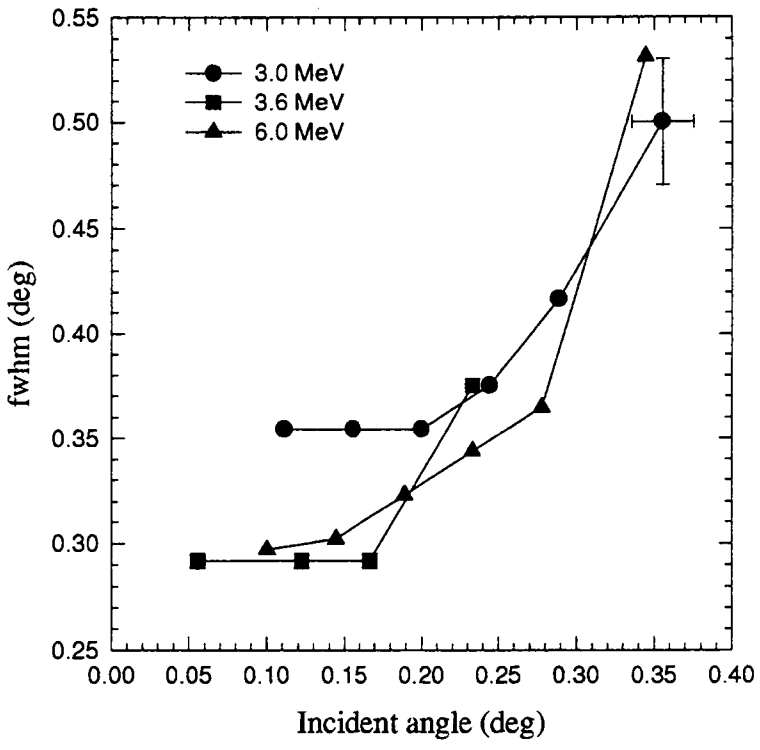

Figure 4.5: FWHM of peaks vs. incident angle

Earlier in this section the increase of the widths with increasing angle of incidence was related to multiple scattering resulting from an increased fraction of penetrating trajectories. The existence of a critical angle of incidence may provide a more quantitative description of the onset of projectile penetration of the topmost layer and scattering from deeper layers of the bulk. The values of θ'_{crit} were determined for each projectile velocity and plotted versus $E_p^{-1/2}$ as shown in Fig. 4.6, where E_p is the projectile total kinetic energy.

The figure also shows the fit of the data to a straight line of the form

$$\theta'_{crit} = AE_p^{-1/2} + B, \tag{19}$$

with slope given by $A = 590.7°\text{eV}^{-1/2}$ and intercept point $B = -0.14°$. The linear re-

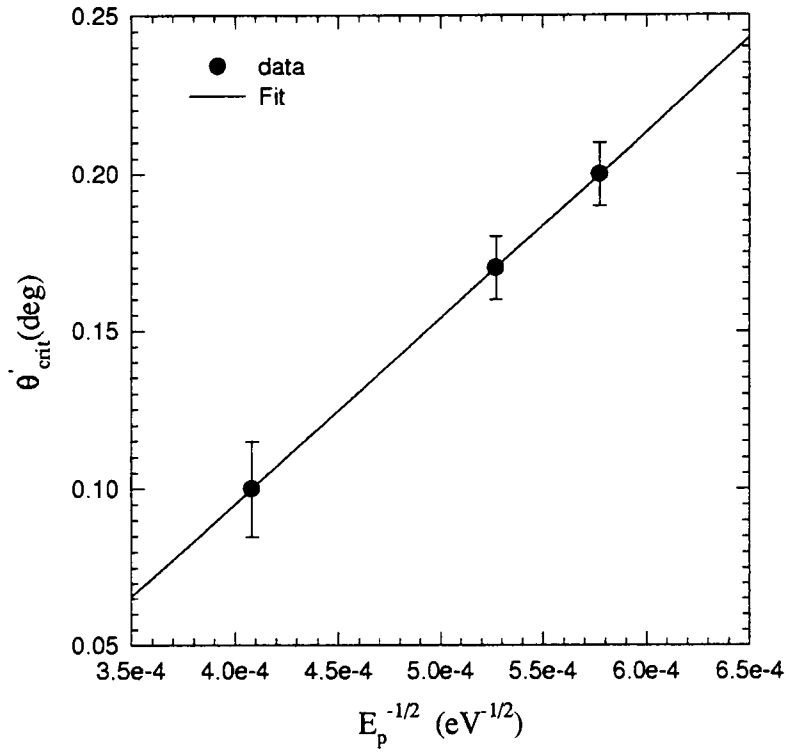

Figure 4.6: Critical angle vs. $E_p^{-1/2}$ ($\mathrm{eV}^{-1/2}$)

lation observed resembles the relation between the critical angle for non-penetrating trajectories for a given projectile energy discussed in connection with equation 5 (section 2.2). For an ion with energy E_p the critical angle for not penetrating the surface layer, derived from equation 5, is

$$\theta_{crit} \approx \frac{\sqrt{V_{planar}(x=0)}}{\sqrt{E_p}}. \tag{20}$$

Equation 19 however includes a constant term B as opposed to equation 20. This can lead to two possible interpretations: Assuming the model described by equation 20 to be correct the small non-zero value of B obtained from the fit could be attributed to a systematic error in the measurements leading only to a constant shift of all the the data points shown in Fig. 4.6. The other possibility would be to consider the

model derived from equation 5 to be incomplete in which case the non-zero value of B could represent a small contribution missing in equation 5.

Considering the first interpretation to be true *i.e.* assuming that the model described by equation 20 is valid, a systematic error could rise from the determination of the absolute value of the zero degree angle of incidence. Even though the precision with which the position of the angle of incidence can be reproduced is better than 0.05°, the error in the measurement of the absolute value of zero degree can be larger and is plausible that it could be of the order of 0.1°. Such error however leads only to a constant shift of the data points shown in Fig. 4.6 but does not affect the determination of the value of the slope A of the straight line that fits the data points. Furthermore the such good linear relation followed by the data points as observed in Fig. 4.6 suggest that the slope is well defined and that is not affected by the systematic error affecting B, which only has the effect of shifting all the data points by a constant value. In this sense and in order to extract then information from the slope A, the small non zero value of B can be assumed to be B=0 so that equations 19 and 20 can be compared. By comparing the slopes of both equations, a value for the V_{planar} at the surface ($x = 0$) can be obtained as $V_{planar}(x = 0) = A^2$. For $A = 590°\text{eV}^{-1/2}$ this results in a measured value of $V_{planar}(x = 0) = 106 \pm 35$ eV.

The error bar of the measurement of $V_{planar}(x = 0)$ of 35 eV results from calculating the possible lines that can go through the error bars indicated in Fig. 4.6. The measurement of A and therefore of $V_{planar}(x = 0)$ is mainly dominated by the precision of the measurement of the outgoing angle. The error of the measurement could be reduced if a position sensitive detector would be used instead of the present ion detector, since the entire angular distribution could then be measured simultaneously avoiding distortions in the shape of the distributions that result from fluctuations in the beam current. The present experimental setup was geared towards performing coincidence measurements of electrons with the scattered ions, and for this reason an electron multiplier was used to detect the ions to allow higher coincident event

rates than could be obtained by using a position sensitive detector. Even though the measurement could be improved, the present measurements lead to interesting observations as shown in Fig. 4.5.

The value predicted for $V_{planar}(x = 0)$ using the Moliere planar-averaged potential (equation 3) is $V_{planar}^{theory}(x = 0) = 117$ eV, assuming $Z_P = 6$. Using equation 3, the value of Z_P which would reproduce the measured $V_{planar}^{exp}(x = 0)$ would be $Z_P = 5$ indicating a difference with the calculated values. This difference may result from the approximation used for the static screening assumed in the calculation of V_{planar} suggesting that further refined measurements of the angular distributions could provide some insight in the calculation of a dynamical screening of the incident ion by the surface atoms.

Careful study of the angular distribution widths vs. incident angle therefore provides a method to determine the critical angle of incidence at which a fraction of the incident ions penetrate the surface for a given projectile velocity.

4.3 Charge state Fractions

When a beam of particles with incoming charge q_{in} traverses a target of thickness z, a distribution of charge states exiting the foil will be produced which does not change for targets thicker than an equilibration value z_{eq}. Alternatively for targets with thickness $z > z_{eq}$, exiting charge state distributions are independent of the incoming charge state of the ion.

The above observations are interpreted, e.g. in ref. [44], in the following way: The charge state of an ion that passes through a thin solid foil target fluctuates due to competition between electron capture and electron loss processes. As a result of this competition, and after a sufficiently large but finite number of interactions with target atoms, the charge of the ion tends toward an asymptotic value referred to as *equilibrium charge state.* The corresponding exiting charge state distributions for

ions exiting a foil with thickness $z > z_{eq}$ are referred to as *equilibrium charge state distributions.*

All projectile ions with varying initial charge states q_{in} transverse the same path length throughout the collision corresponding to the target thickness z. In the case of an ion interacting with a surface at grazing incidence the scattering geometry is very different. A naive prediction would be that an ion could get closer to the surface the smaller the incident charge state due to less repulsion provided by the top most layer of atoms. Therefore ions with varying q_{in} would travel a different path length z^{surf} along the surface, *i.e.* $z^{surf} = z^{surf}(q_{in})$, as opposed to what happens under normal incidence conditions. Furthermore, under grazing incidence an equivalent definition of equilibration target thickness, z_{eq}^{surf} would then turn out to be incoming charge state dependent. Based on this simple model exiting charge state distributions in ion-surface collisions could be expected to be dependent of the charge state of the incident ion.

Fig. 4.7 shows outgoing charge state distributions produced by various $C^{q_{in}+}$ ions at a total kinetic energy of 6.0 MeV incident at a grazing angle of 0.15° and scattered by a silicon surface. Interestingly the charge state distributions are independent of the incoming charge state implying that the ions have reached charge state equilibrium. The same is observed for the entire projectile velocity regime studied. This can be interpreted in terms of the number of target atoms encountered by the ion.

The equilibration thickness for 6.0 MeV projectiles transmitted through an amorphous carbon foil is $z_{eq} \approx 20$ nm [41]. The number of atoms then encountered by an ion is $N \approx 56$ atoms, estimated as $N = z_{eq}/a$ where $a = 3.57$ Å is the average separation between atoms in amorphous carbon. Similarly in the grazing incidence case the number of atoms encountered by the projectile ion can be estimated from geometry considerations in the following way: Assuming that the ion starts changing charge when it is at about 3 a.u. [18] above the surface and that the distance of closest approach is ~ 0.5 a.u. the total ion path length along the surface would be

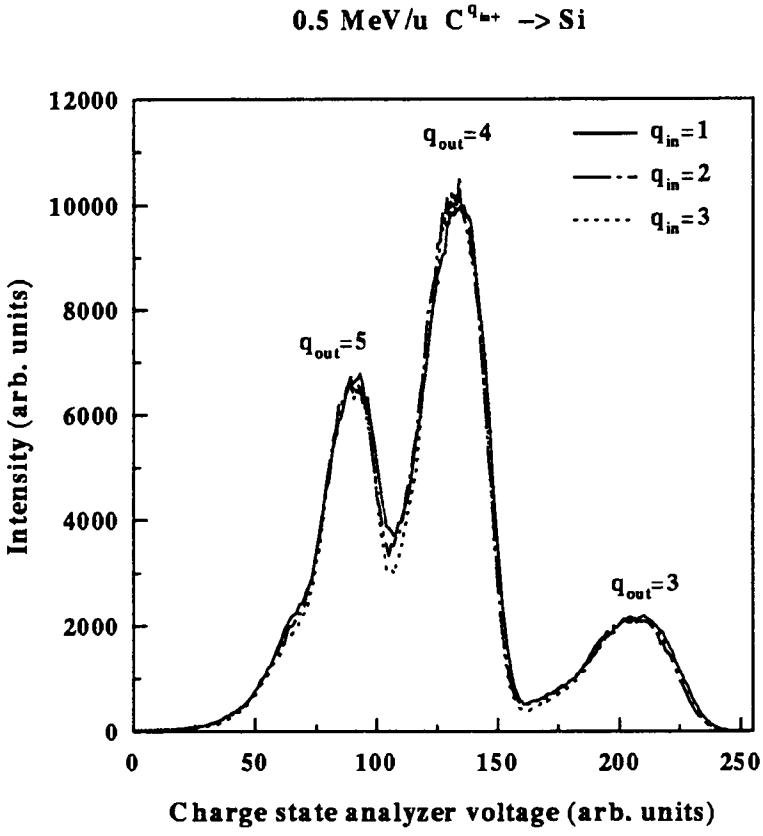

Figure 4.7: Charge state equilibration

$z = 120$ nm. Since the spacing between target atoms in silicon is $a = 5.43$Å the number of atoms encountered by the ion would be $N = 220$, indicating that the ion encounters enough collisions to equilibrate its charge.

To further investigate the charge changing process in ion-surface collisions we have compared charge state distributions produced by carbon ions scattering at grazing incidence from a silicon surface with ions transmitted through a 20 ug/cm^2 carbon foil. Outgoing charge state distributions for both cases are shown in Fig. 4.8 for several projectile energies. Several observations can be made directly from the raw data. The various charge state components shift towards a higher value for increasing projectile velocity in both cases as expected in foil-transmission experiments. The

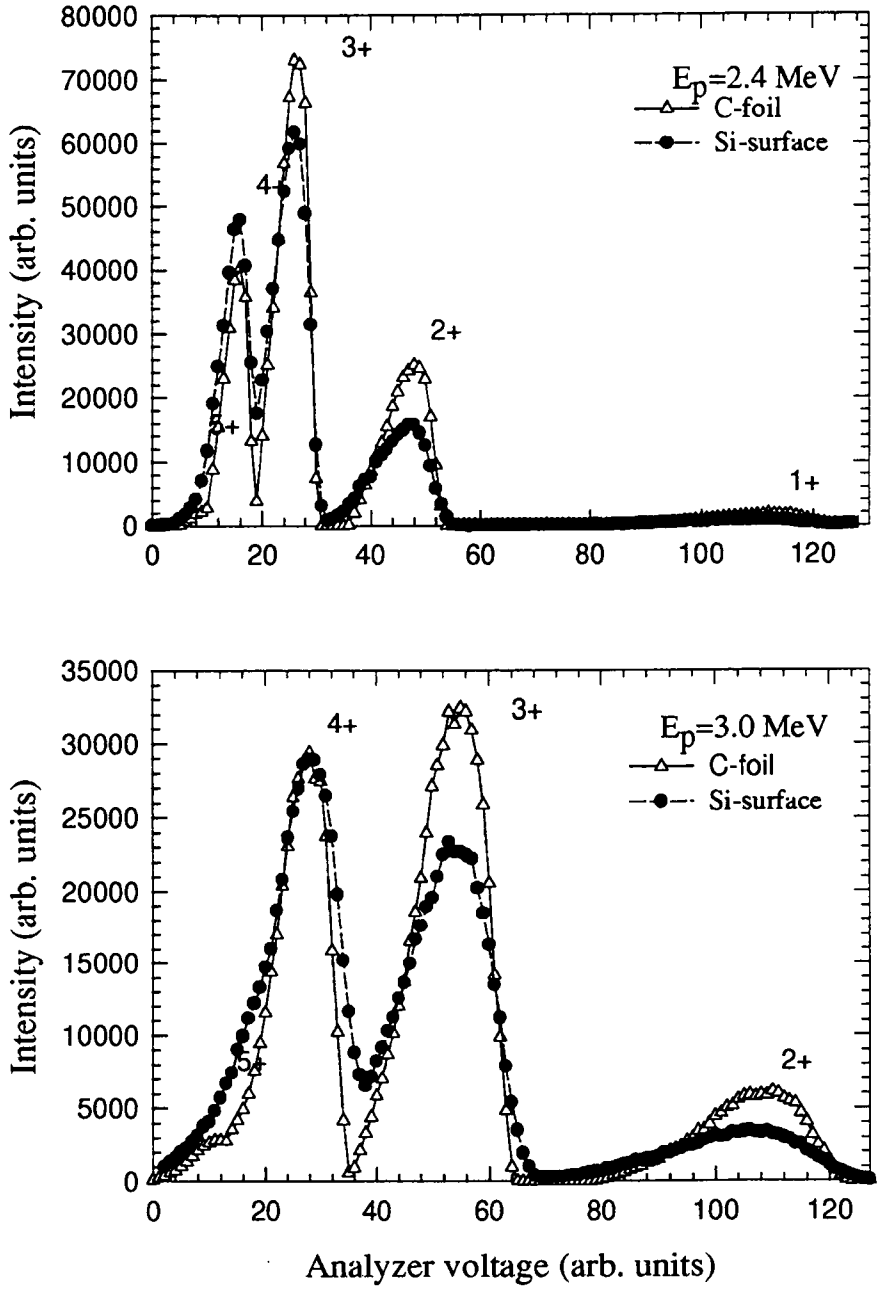

Figure 4.8: Raw outgoing charge state distributions for several projectile energies

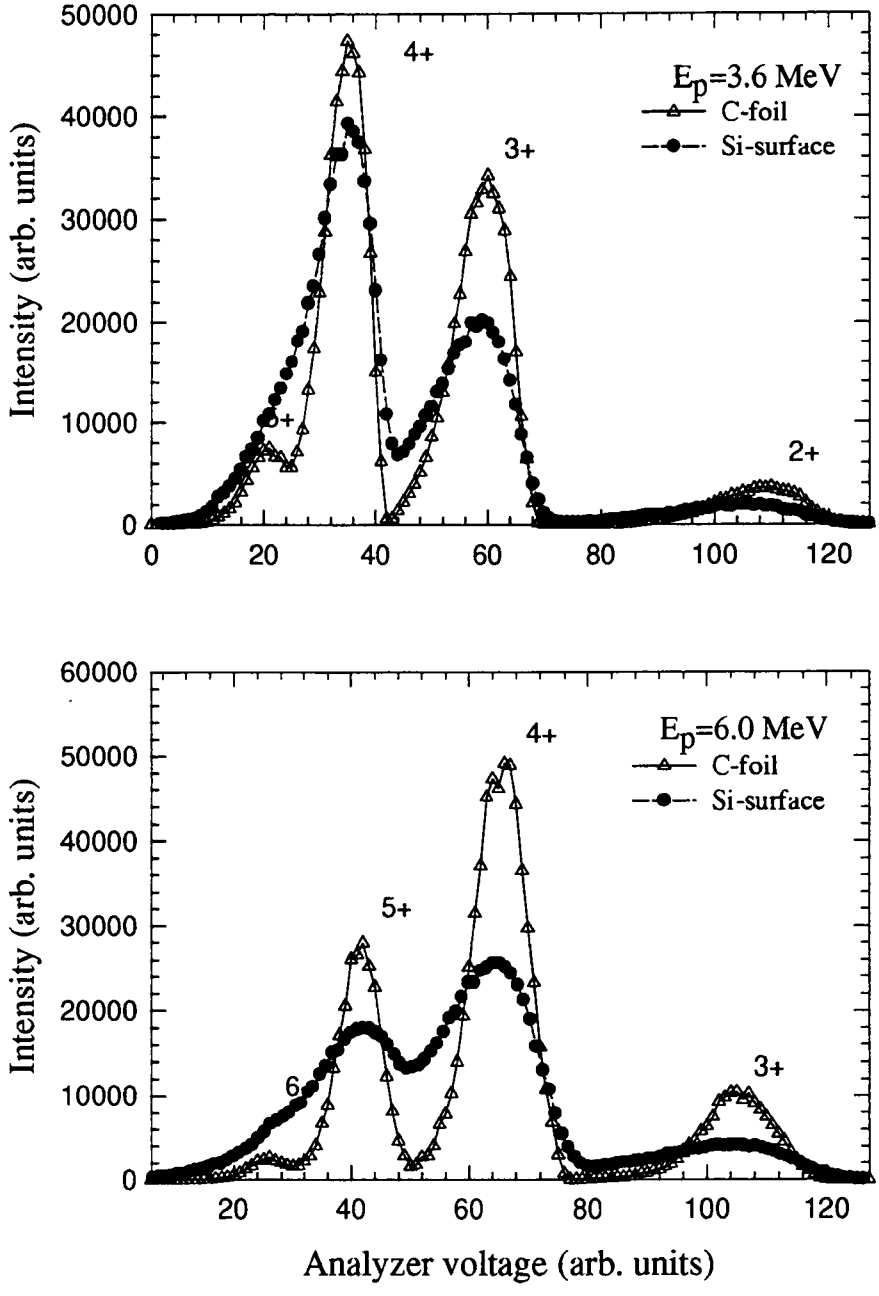

Figure 4.8: (continued)

widths of the peaks produced under grazing incidence are broader. Since the geometry of the apparatus is the same for the grazing and normal incidence experiment a broadening of the peaks could result due to a broader energy distribution of the ions scattering from the surface compared to the case of the ions exiting the thin carbon foil.

From the spectra shown in Fig. 4.8 the equilibrium charge state fractions,$\{F_q\}$ were obtained for all projectile velocities as

$$F_q = \frac{A_q}{\sum_q A_q}, \tag{21}$$

where A_q is the area under the peak corresponding to exiting charge state q after dividing the charge state distribution by the voltage applied to the charge state analyzer. The division by the charge state analyzer voltage takes into account the instrumental broadening of the peaks, which increases for smaller charge states. In order to calculate the areas a fitting routine was used that allowed deconvoluting the peaks. Typical fits are shown in Fig. 4.9. The model function used is shown in the inset of Fig. 4.9b), and corresponds to the peak in the spectrum with lower charge state, which is well separated from the remaining part of the spectrum. Using a scaled version of this model function the various peaks could be successfully fit as opposed to earlier unsuccessful attempts in trying to use analytical expressions such as asymmetric Gaussians or Voigt (convolution of a Gaussian and Lorentzian) functions.

The charge state fractions, $\{F_q\}$, for all projectile velocities are plotted in Fig. 4.10. The number of events acquired in the spectra was large enough to reduce the statistical error to less than 1 %. The widths of the $\{F_q\}$ distributions of the ion-surface and the ion-foil cases are very similar which may indicate that the charge changing mechanisms are similar in both situations. However, the ion-surface $\{F_q\}$ distributions are shifted towards higher exit charge sates at each impact energy. To

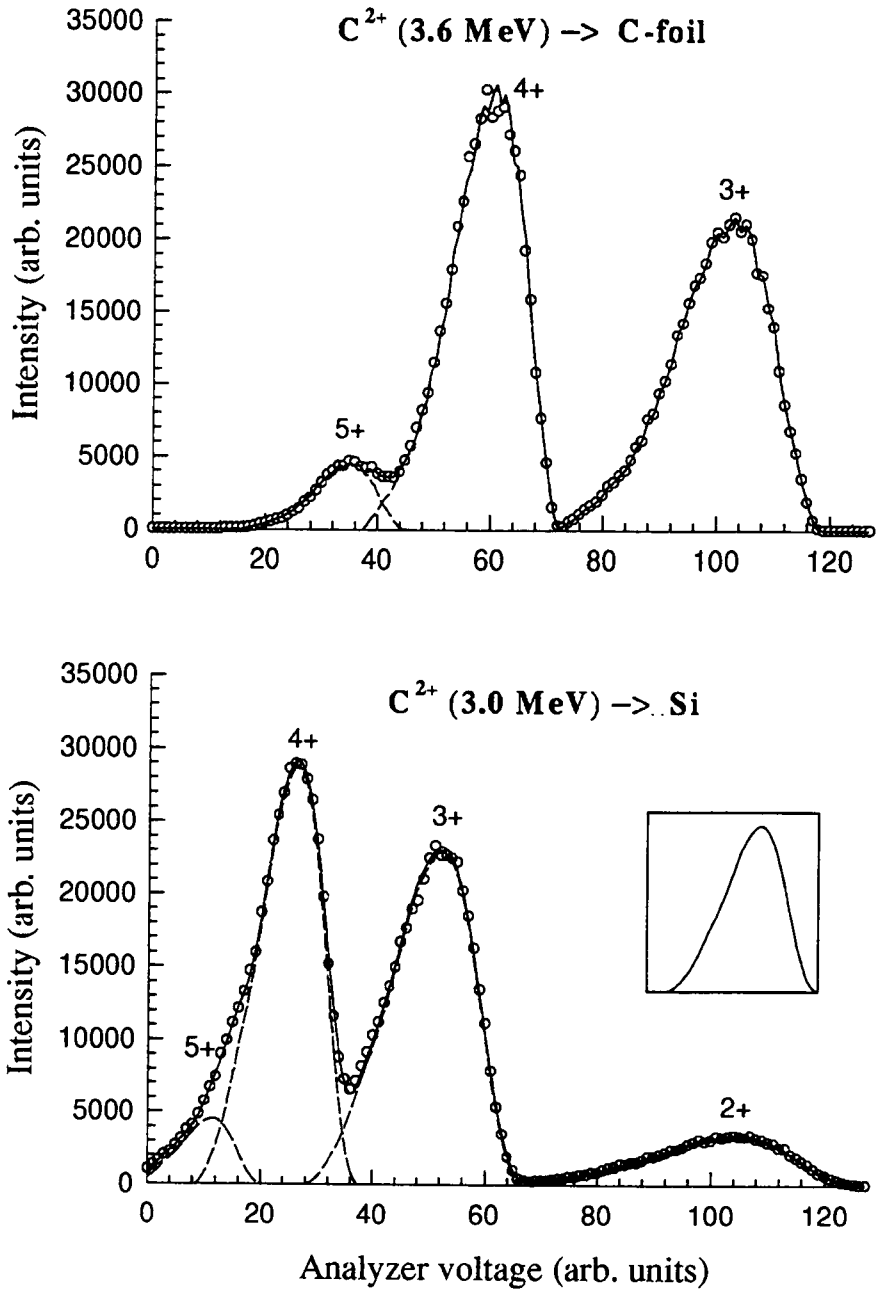

Figure 4.9: Fit to data

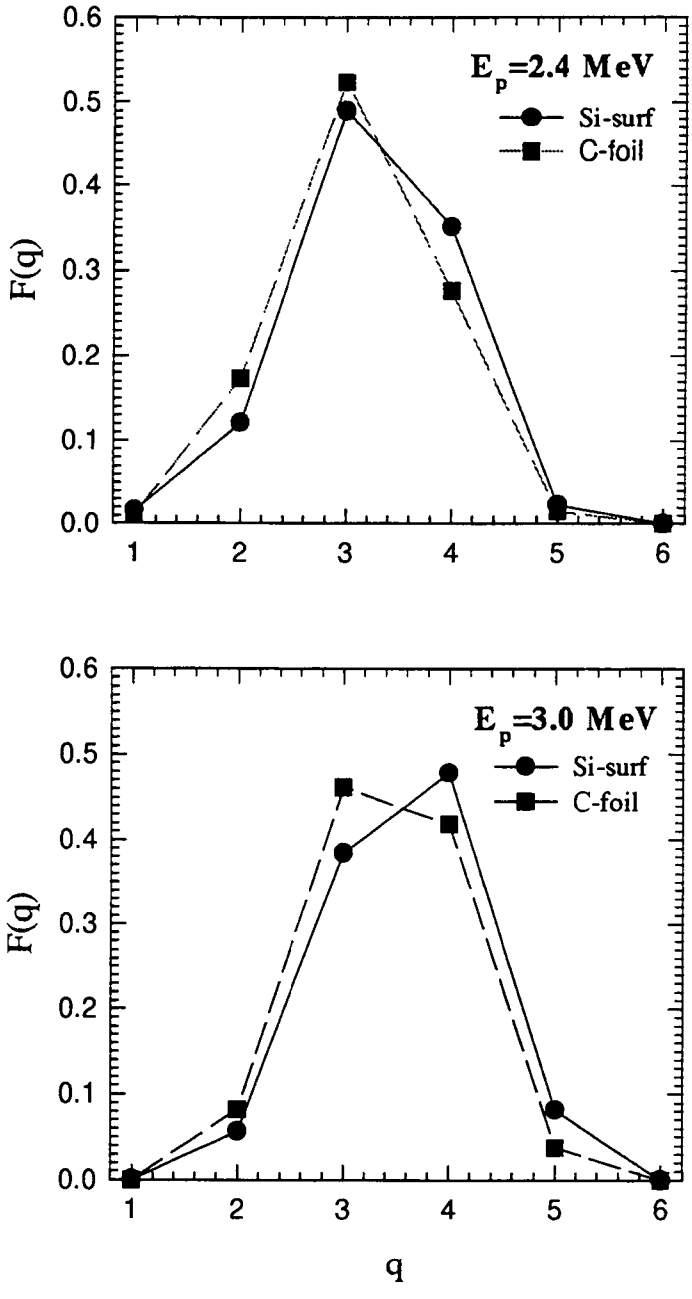

Figure 4.10: Charge state fractions

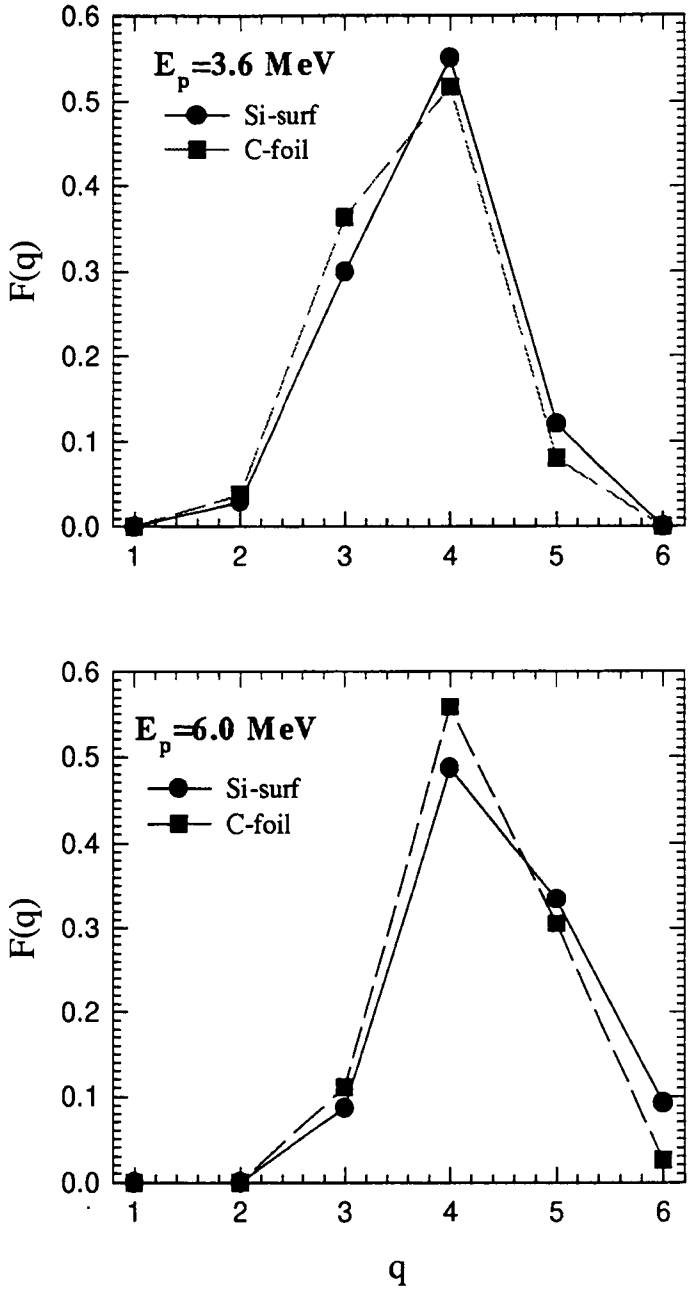

Figure 4.10: (continued)

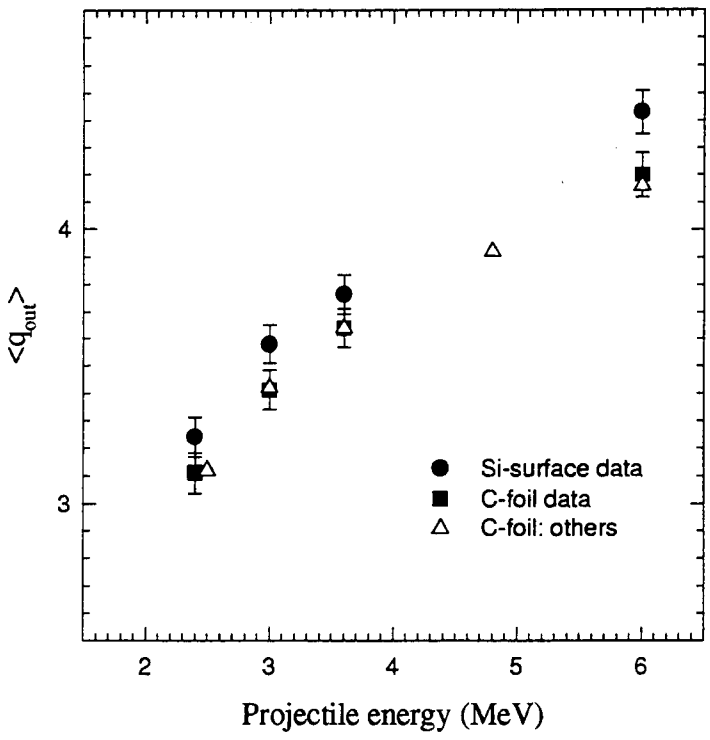

Figure 4.11: Average exit charge vs. projectile impact energy

further quantify this, the mean exit charge was calculated for all projectile energies as

$$< q >= \sum_{q} qF_q, \tag{22}$$

and is shown in Fig. 4.11. The figure indicates that the average exit charge state is larger in the case of grazing incidence collisions compared to normal incidence. In addition the figure shows other experimental data produced by carbon ions transmitted through a carbon foil [42, 43]. Our data is in good agreement with the results obtained previously indicating that there are no systematic errors in the measurements of the charge state distributions. Ideally the comparison of the fractions obtained under grazing incidence should be made with carbon ions transmitted through silicon

rather than through carbon foils. Unfortunately to my knowledge no measurements have been reported, [43] most likely due to difficulties in making self-supporting silicon foils. In the compilation by Shima *et al.* [43], however, results from measurements of oxygen ions transversing carbon and silicon foils at a projectile velocity similar to the one used in our experiment are reported. The mean exit charge for 8.8 MeV ions transmitted through a carbon foil is $< q_{out} >= 5.61$ compared to the value of $< q_{out} >= 5.35$ resulting from ions transmitted through a silicon foil. Assuming that the difference in the value for $< q_{out} >$ for silicon compared to carbon is also observed for carbon projectiles, the mean exit charge of carbon ions scattered at grazing incidence from a silicon surface would be larger than ions transmitted through a silicon foil. Furthermore, the difference between grazing and normal incidence conditions, would be larger than the one observed when comparing the results of ions interacting with the silicon surface and carbon foil as shown in Fig. 4.11.

The remarkable differences observed between the grazing and normal incidence charge state distributions seen in Fig. 4.8 are not quite as evident in the mean exit charge $< q_{out} >$ plotted in Fig. 4.11. A more dramatic measure of the difference between surface and foil collisions is provided by the ratio F_3/F_4, which has been graphed in Fig. 4.12 for all projectile velocities. From this figure it becomes more apparent that the surface effect increases with lower projectile energies.

The evolution of the charge state fractions inside a solid of thickness z can be expressed by the system of rate equations

$$\frac{dF_i}{dz} = \sum_j (F_j \sigma_{ji} - F_i \sigma_{ij}), \tag{23}$$

where $i, j = 1, 2...Z_P$ and σ_{ij} are cross sections for electron capture and loss. If charge state equilibrium is achieved for $z > z_{eq}$ the fractions $\{F_q\}$ become stationary, or

$$\frac{dF_i}{dz} = 0. \tag{24}$$

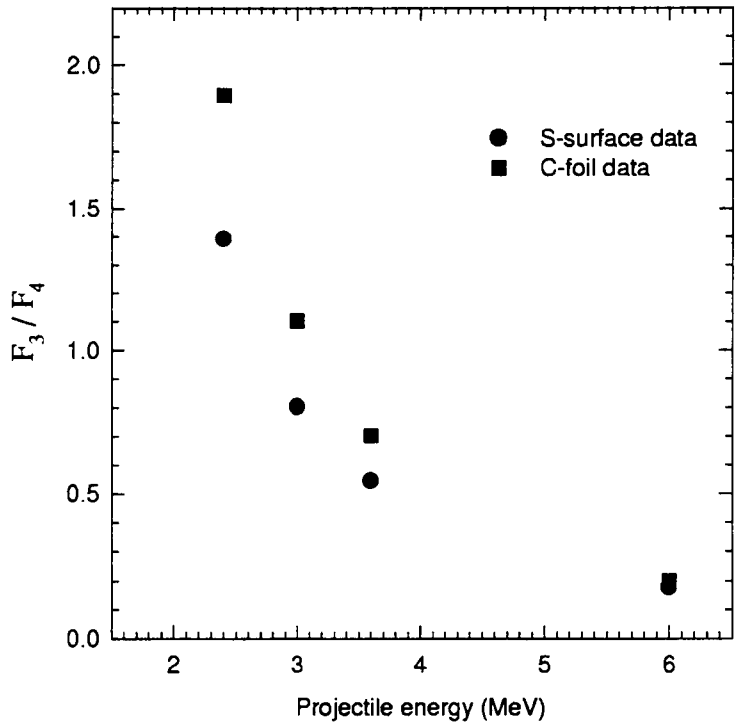

Figure 4.12: Ratio of fractions F_3 and F_4

For an ion passing through a foil the total cross sections that appear in equation 23 have a single value. An ion-surface collision is more complicated. The cross sections must be replaced by probabilities which depend on the distance from the surface. A theoretical calculation of the charge fractions would then involve calculating the probabilities for electron capture and loss. Calculations of distance dependent probabilities have been calculated for other collision systems e.g. in [18], however such a calculation hasn't been performed for this particular collision system, *i.e.* for carbon ions interacting at grazing incidence with a silicon surface. In the following paragraph a prediction is made about how the probability for electron loss in grazing and normal incidence collisions would compare, and the effect on F_i.

The probability of ionizing a projectile electron is maximized if the impact parameter is equal to, or smaller than, the electron orbital radius, otherwise the ionization

probability decreases. The radius of the $1s$, $2s$, and $2p$ orbitals in carbon are 0.3, 1.5 and 1.8 a.u., respectively. At the velocities used the distance of closest approach varies between 0.4 and 0.7 a.u. In the particular case that an ion interacts with a one-dimensional array of atoms, an ion traveling within a distance of 1.8 a.u. from the surface will only access values of impact parameters smaller than 1.8 a.u. In the more general case in which the ion interacts with a surface only the component of impact parameter that is perpendicular to the surface will access impact parameter values smaller than 1.8 a.u. In the case of an ion passing through a thin carbon foil instead the value of impact parameters accessed by the ion is done randomly and over a wider range, approximately between $b \approx 0$ and $b_{max} \approx a/2 = 3.37$ a.u. (where a corresponds to the average spacing between carbon atoms). Furthermore larger impact parameters have a larger access probability assuming that the probability of accessing impact parameters between b and $b + db$ is proportional to $\pi b db$. The differences above mentioned would suggest that an electron in a carbon ion could have a larger probability of being ionized in the grazing incidence interaction.

The above paragraph considers only the contribution to the total ionization probability originating from the interaction of the projectile electron with the target nucleus. The ionization due to surface electrons interacting with the ion also contributes to the total probability. Even though the projectile electrons also are ionized, under normal incidence conditions, resulting from the interaction with target electrons in the bulk solid, the effect may be larger under grazing incidence since as the ion recedes from the surface the electron impact ionization mechanism may dominate over electron capture at distances away from the surface.

An increase of the ionization probability in the grazing incidence case would lead to a shift of the charge state fraction distributions to a larger q value. However the above arguments excludes the comparison between grazing and normal incidence for the capture probabilities. A simple prediction cannot be made since it would require knowing the relative contribution from the different target shells of electron

capture to a bound state of the projectile. A prediction based on only velocity matching arguments could lead to the wrong conclusion as will be discussed in the next chapter for the similar case of electron capture to the continuum.

5 Electron emission

5.1 Overview

Results associated with the electron emission measurements are presented in this chapter, which is divided into four sections. The first section presents electron emission spectra in which the two prominent structures, the convoy peak and binary shoulder, are discussed. Surface effects which have been previously observed in other collision systems are confirmed. The main focus of the discussion is on the effect the surface has on the convoy peak *i.e.* the shift and broadening of the peak. The second section presents absolute measurements of electron spectra with main focus on the first reported determination of absolute yields for convoy electron emission produced in ion-surface collisions. From the velocity dependence of the yields and by comparison between experiment and theory, it is possible to provide new insight into the origin of convoy emission. In brief, it is found that convoy electrons originate from competing capture of core and valence electrons, and that the relative contribution of each emission is sensitive to target species. The third section addresses the question of where convoys and binaries go in ion-surface collisions; *i.e.* the question of their angular distribution. It is observed that convoy electrons are emitted along trajectories that lie closer to the surface than binary encounter electrons. Finally, the last section discusses an observed incident charge state dependence of the shift of the convoy peak.

The measurements presented in this chapter correspond to carbon projectile ions with charge states $q = 1, 2, 3, 4$ and total kinetic energies of 3.6 MeV and 6.0 MeV. The electron emission spectra presented were measured in coincidence with specularly reflected ions from the silicon(100) surface and in a given exit charge state.

5.2 Surface effects on electron emission

The collision and electron emission geometry is described as follows: The surface target lies in the (y,z) plane and the projectile is incident in the (x,z) plane: The incident projectile velocity vector is inclined at an angle θ_{in} with the z-axis *i.e.* $\hat{v}.\hat{z} = \cos\theta_{in}$. The emitted electrons are characterized by their energy and two emission angles θ_x and θ_y. Using this convention the electron velocity can be expressed as $\vec{v}_e = (v_x, v_y, v_z)$ and the two angles defined more precisely as $\theta_x = tan^{-1}(v_x/v_z)$ and $\theta_y = tan^{-1}(v_y/v_z)$. The intensity, $N(E, \delta E, \Omega, \delta\Omega)$, represents the number of electrons measured in the energy interval $(E - \delta E/2, E + \delta E/2)$ and solid angle interval $(\Omega - \delta\Omega/2, \Omega + \delta\Omega/2)$ where, as explained in chapter 3, δE and $\delta\Omega$, given by $\delta\Omega = \delta\theta_x\delta\theta_y$, are the energy and angular resolution of the electron spectrometer.

Fig. 5.1 illustrates typical features of the raw energy electron emission spectra produced by projectiles with total kinetic energies of 3.6 and 6.0 MeV. The spectra were obtained by measuring the electron distributions in coincidence with outgoing C^{4+} ions scattered in the specular direction. The distributions shown in the figure were obtained by integrating the intensity, given by $N(E, \delta E, \Omega, \delta\Omega)$, over a narrow range of emission angles $2° \leq \theta_x \leq 11.0°$ and $-5° \leq \theta_y \leq +5°$. Two distinct populations can be observed at the two projectile energies. For example, the electron spectra produced by 6.0 MeV carbon ions show a convoy peak at $\sim$ 320 eV produced in electron capture and loss to continuum processes, and binary encounter electrons, in the range 600 to 1000 eV, produced in direct collisions of the projectile with target valence electrons ($E_{bin} = 2v_p^2$ indicates the approximate position of the binary peak observed in ion-atom collisions). The convoy peak is shifted by about 50 eV with respect to the cusp position $E_{cusp} = v_p^2/2$ (atomic units) which would be expected for convoy electron emission in ion-atom and ion-foil collisions. As mentioned in the introduction, the shift of the peak has been observed for several collision systems [7, 8, 10, 12, 13] and has been interpreted as resulting from a repulsion caused by the surface-wake or dynamic image potential induced by the moving ion.

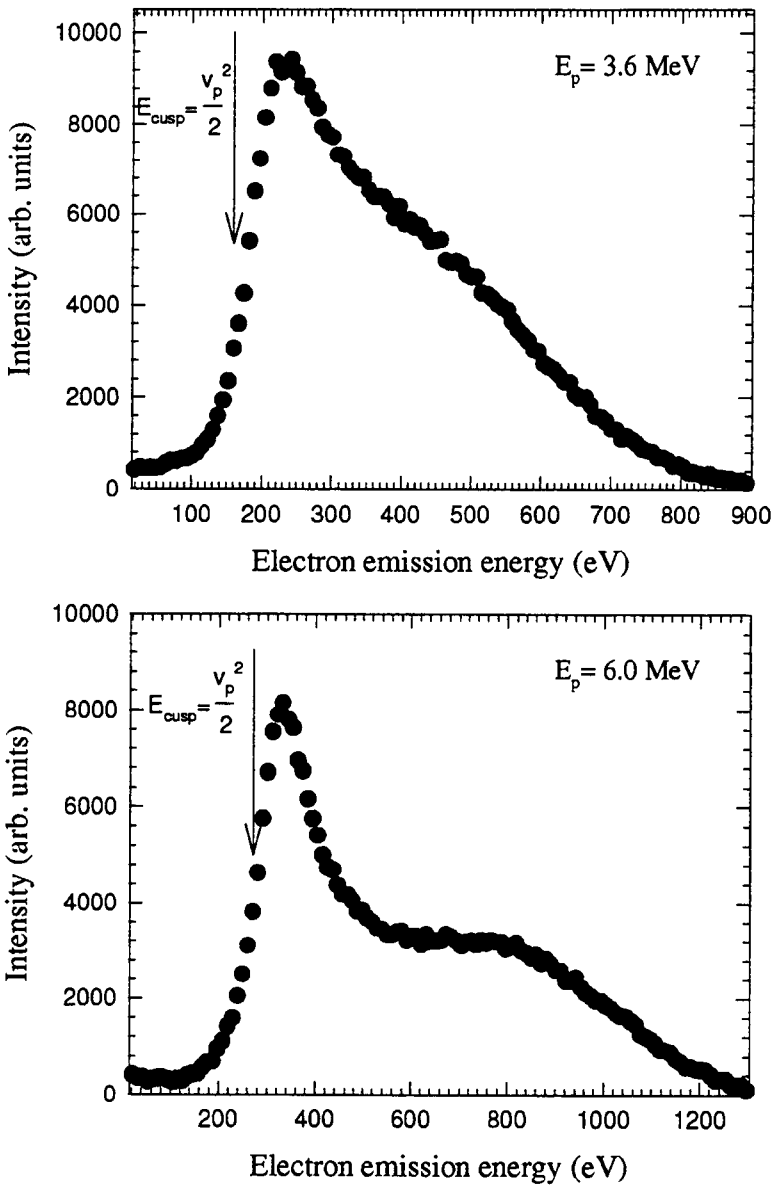

Figure 5.1: Energy distributions produced by 3.6 MeV (top) and 6.0 MeV (bottom) C^{1+} ions scattering upon a silicon surface at 0.15°.

Fig. 1.1, shown in chapter 1, displays explicitly the effect of the surface on the convoy peak, as seen in the energy spectrum, by comparing two spectra produced by the same projectiles under normal and grazing incidence. Note in that figure, however, that in the normal incidence case the target was a carbon foil and for the grazing incidence case, corresponded to a silicon surface. This implies that a detailed comparison between the two spectra is not appropriate. Nevertheless, the shifted position of the surface convoy peak, which is clearly observed in Fig. 1.1, corresponds to a surface effect. In addition, the surface peak becomes much broader than that observed in transmission foil experiments. The broadening is also thought to result from the interaction of the emitted electrons with the surface wake [17]. Mainly electrons captured to the projectile continuum with different energies are subjected to different accelerations leading to a broader peak. The wake potential resulting from the polarization of surface electrons is formed by two contributions *i.e.* polarization of core and of valence electrons from the target. Reinhold *et al.* [18] have found through their simulations that the main contribution to the broadening of the peak is due to polarization of core electrons in the surface.

The presence of the surface-wake is manifested not only in the energy distribution but also in the angular distribution of convoy electrons. Fig. 5.2 displays an angular distribution corresponding to the same collision system given in Fig. 5.1b) and was obtained by integrating the intensity over the approximate FWHM of the convoy peak, $262 \leq E \leq 449$ eV and $-5° \leq \theta_y \leq +5°$. In addition, an angular distribution of electrons produced in collisions of carbon ions transmitted through an amorphous carbon foil is shown in the figure. In the latter case the angular distribution peaks in the forward direction *i.e.* along the outgoing beam direction. Notice that, in the transmission foil collision case, the cusp-like behavior of the convoy peak as observed in the energy spectrum is also seen in the emitted electron angular distribution, indicating the well-known fact that the cusp-divergence occurs in the triply differential emission rather than solely in the singly differential (in energy) emission. The ion-

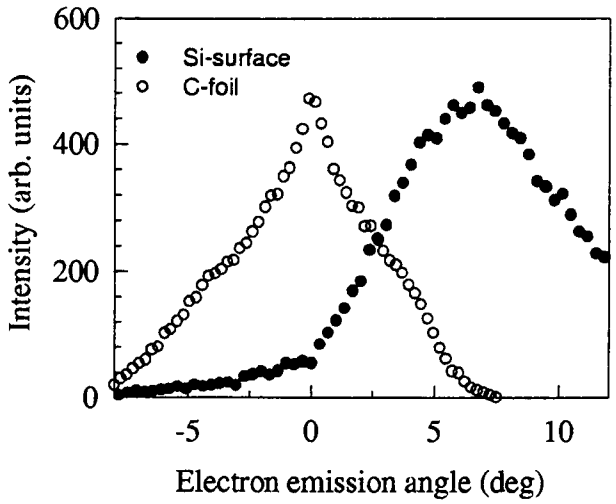

Figure 5.2: Angular distributions produced by 6.0 MeV C^{2+} ions incident at 0.15° on a silicon surface (solid circles) and transmitted through a 20 ugr/cm^2 carbon foil (hollow circles).

surface angular distribution peaks at a few degrees away from the surface plane due to the repulsive effect of the surface wake. The effect of the surface is remarkable when compared to the distribution produced in ion-foil experiments which peaks in the forward direction as shown in Fig. 5.2. At small values of θ_x corresponding to electron emission nearer the surface than the peak, the number of events is very small since for such emission angles the electrons would either pass slightly above the surface and would become attenuated by multiple collisions with the valence electron selvage, or enter the crystal and become lost to multiple collisions within the bulk. The presence of the small tail for small negative θ_x is not completely understood.

Fig. 5.3 shows the emission spectrum produced by C^{2+} ions incident at various incident angles. The position of the peak remains almost unchanged. The perpendicular energy associated with an incident angle of $\theta_{in} = 0.4°$ is $E_{perp} = 292$ eV which indicates that some ions penetrate the topmost layer of the surface, given the surface planar-averaged potential estimated in the chapter 2 ($V_{planar}(x = 0) \approx 120$

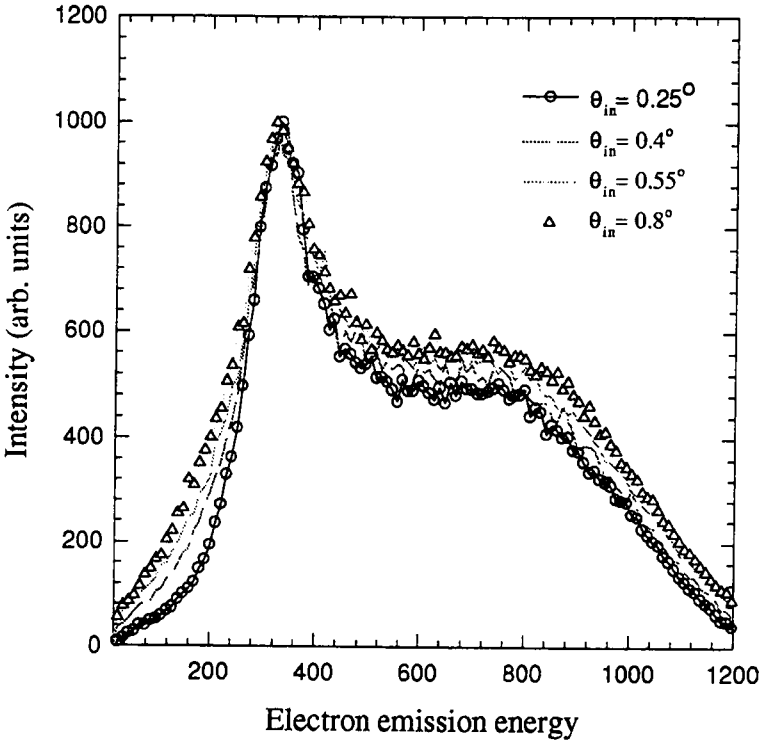

Figure 5.3: Energy distributions of electrons produced by 6.0 MeV C^{3+} ions incident at various angles of incidence: $0.25°, 0.4°, 0.55°$ and $0.85°$.

eV). The existence of an accelerated peak associated with trajectories penetrating further than the topmost layer would mean that the wake associated with the bulk induced by the moving ion plays an important role in the acceleration of the emitted electrons. A bulk-wake accelerated peak has also been observed using a different projectile-target combination by Koyama *et al.* [8] in which 13.72 MeV N^{6+} ions were incident at $\theta_{in} = 1°$ on an aluminum surface. The perpendicular energy in that work was $E_{perp} = 4178$ eV, a much larger value than the planar-averaged Moliere potential surface barrier $V_{planar}(x = 0) = 182$ eV.

Although the peak position remains unchanged, some differences are observed in the electron spectrum for increasing incident angle, mainly an increase in the convoy peak width and in the intensity of the background of low energy secondary electrons.

The increase in the width would be consistent with electrons produced deeper inside the solid and therefore subjected to a larger amount of multiple scattering processes prior to exit from the surface.

By comparing Fig. 5.2 and Fig. 4.5 it can be concluded that there is little causal connection between the remarkably broad electron angular distribution and the angular distribution of ions scattered from the surface. Typical widths for electron distributions are about $\sim 9°$ (FWHM), much larger than the corresponding case of widths smaller than $0.4°$ for the scattered ions. This means that the narrow width of the scattered ion angular distribution can not be responsible for the broadening of the convoy peak angular distribution. Consequently the observed large width of the electron angular distribution points to the interaction of the electrons with the surface as being responsible for such broadening, i.e. the interaction of the electrons with the surface wake. A similar lack of connection between the energy distribution of emitted electrons and that of scattered ions has been observed. For 6 MeV carbon ions the typical width of the convoy peak is 120 eV (about 45% of the peak position) in contrast with a typical 3% energy loss for ions scattering from surfaces [17].

5.3 Measurement of absolute electron emission spectra

In the previous section the main effects of the surface on the electron emission spectrum were discussed with a main focus on convoy emission. As has been discussed the wake is responsible for the shift and broadening of the convoy peak as seen in both the angular and energy distribution of emitted electrons. Nothing has been said until now regarding the origin of convoy electrons in ion-surface collisions. This section addresses this matter by making a comparison of measured absolute yields of convoy electrons, performed as part of this dissertation [14], with results obtained from a recently developed CTMC simulation by Reinhold and Burgdörfer [18] describing electron emission in grazing incidence ion-surface interaction.

In order to be able to make such a comparison an observable common to experi-

ment and theory must be used. Such an observable is the differential yield of emitted electrons per ion, per unit energy, and per unit solid angle which will be denoted $\frac{d^3N}{dEd\Omega}$. The differential yield is related to the number of electrons detected, N, (or intensity) by means of a convolution over the experimental resolution described by the spectrometer transmission function $T(E, E', \Omega, \Omega')$ [45, 46] and can be expressed as

$$N(E, \delta E, \Omega, \delta\Omega) = N_p \int_{\delta E} \int_{\delta\Omega} \frac{d^3N}{dEd\Omega}(E', \Omega')\epsilon T(E, E', \Omega, \Omega')dE'd\Omega', \qquad (25)$$

where ϵ represents the detector efficiency and N_p is the total number of specularly scattered projectiles detected in a given exit charge state. Assuming that the differential yield varies slower than the spectrometer resolution function within an interval δE and $\delta\Omega$ the differential yield, $\frac{d^3N}{dEd\Omega}$, can be factored out of the integral. The remaining integral over the spectrometer transmission can be solved in terms of an average over the spectrometer energy and angular resolution, δE and $\delta\Omega$, resulting in the following expression for the differential yield in terms of the measured observables

$$\frac{d^3N}{dEd\Omega}(E, \Omega) = \frac{N(E, \delta E, \Omega, \delta\Omega)}{\epsilon \bar{T} N_p \delta E \delta\Omega}, \qquad (26)$$

where $\bar{T} = \int_{\delta E} \int_{\delta\Omega} T(E, E', \Omega, \Omega')dE'd\Omega'$ represents the mean value of the transmission function integrated over δE and $\delta\Omega$. The value of the mean transmission efficiency has been taken from a previous simulation that models the present spectrometer, which for the present case corresponds to $\bar{T} = 0.8$ [47]. The detector efficiency ϵ is determined by the efficiency of the channel plates (see section 3.5.1 which, for the electron energy regime studied, corresponds to $\epsilon = 0.6$ [48]. Equation 26 provides an expression to evaluate the differential yield in terms of measured parameters and integrated spectral intensity. In the experiment δE and $\delta\Omega$ correspond to the energy angular resolution of the electron spectrometer. In the case of electron spectra produced by the CTMC simulation [18] $\bar{T} = 1$ and $\epsilon = 1$.

Fig. 5.4 shows a comparison of electron emission spectra produced by C^{2+} ions at two different projectile energies and at an incident angle of $\theta_{in} = 0.15°$ obtained experimentally and from theoretical calculations. The energy distributions were obtained by integrating the differential yield as expressed in equation 26 over the FWHM of the angular distribution as

$$\frac{dN_e}{dE} = \int d\Omega \frac{d^3N}{dEd\Omega}. \tag{27}$$

Note that the integration has been performed only over a finite range of angles therefore leading to a partial singly differential yield as opposed to the case in which the integration is performed over the entire angular range resulting in what is known as the total singly differential yield. To distinguish between these two situations the partial differential yield in the above equation has been denoted by dN_e/dE.

The CTMC simulation used in producing the theoretical spectra shown in Fig. 5.4 has recently been developed by Reinhold and Burgdörfer [18] and describes electron emission in grazing incidence ion-surface interaction. The simulation was applied by Reinhold and Burgdörfer to the present collision system *i.e.* carbon ions on a silicon surface. As described in section 2.4 in contrast with previous models, the simulation takes into account the initial state of the electron in the silicon target. Furthermore, it separates the electron emission in the contribution of valence and core electrons. In the case of silicon the electrons that are considered in the calculation to contribute to the electron emission spectra are the L- and M shell, where the valence band is given by the M shell. For the effective one-electron potential in the solid a muffin-tin potential is used. Depending on its initial binding energy, E_0, with respect to the constant background potential, V_0, an electron can be either localized around an ionic core ($E_0 < V_0$) or move freely in the solid ($E_0 > V_0$). V_0 was chosen to match the top of the valence band of silicon. In previous applications for SnTe surfaces [17, 49], the yield of convoy electrons was dominated by core states of the solid, which are

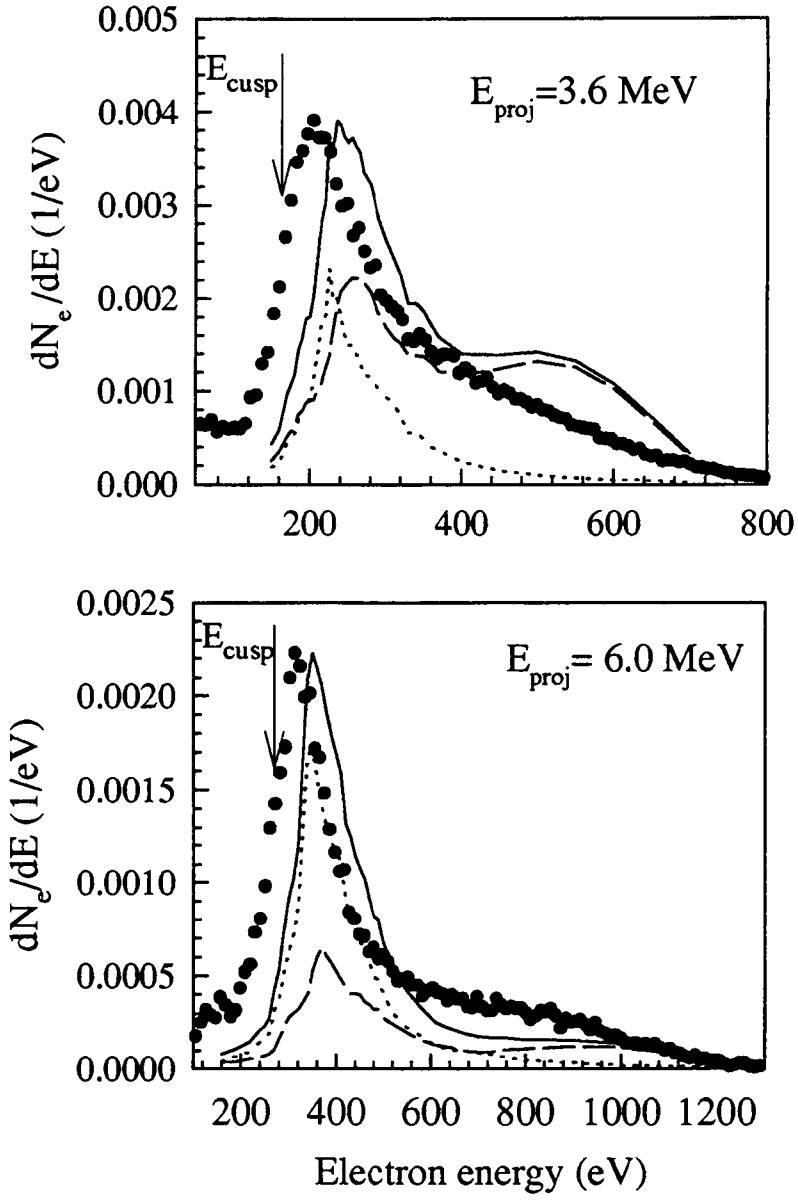

Figure 5.4: The differential electron emission spectrum integrated over an angular region around $2° \leq \theta_x \leq 11°$ and $-5° \leq \theta_y \leq 5°$

well described by atomic-like localized orbitals. Total yields were not very sensitive to the model used to describe valence electrons, treated as free electrons, since their contribution to the yield was small. In the present work, i.e. carbon ions scattering from silicon surfaces, however, valence electrons play a more important role (see valence contribution to the convoy peak in Fig. 5.4). Using the fact that the tight binding approximation describes the electronic structure of silicon reasonably well [50], valence electrons are then treated as localized atomic-like states whose binding energies are approximately given by the main peaks of the experimental density of electronic states [51].

By comparing the experimental and calculated electron spectra as shown in Fig. 5.4, the following observations can be made: Both experiment and theory display a pronounced convoy electron peak which is considerably shifted to energies larger than the cusp energy. The widths are in reasonable agreement but the calculated shifts are slightly larger than the experimental ones. A similar discrepancy between measured and calculated shifts have been previously observed [17]. The authors of the simulation predict that the overestimate of the shift may be a consequence of the classical treatment. Fig. 5.4 shows in addition to the calculated spectra (solid lines) the relative contribution from the M- and L-shell of silicon. Surprisingly, at both projectile energies, there is a large contribution from valence electrons to the convoy peak, as opposed to previous conclusions, derived from experiments using SnTe surfaces [18], that indicated that convoys were produced mainly by capture of core electrons.

Regarding the high energy region of the spectrum the simulation predicts a binary shoulder at $E_{proj} = 3.6$ MeV which is due to valence electrons. This shoulder is not seen in the measurements. As discussed in section 2.5 the measurement of the binary electron peak in ion-atom collisions provides information about the wave function of the electrons in the target or more precisely the Compton profile associated with that wave function. The equivalent binary electron structure observed

in the ion-surface interaction, therefore, will be determined mainly by the momentum distribution of valence electrons in the silicon target. Since binary electrons occur in collisions in which the impact parameter between the projectile nucleus and the electron is very small, it can be treated as a two body scattering problem and is accurately described by classical mechanics (as opposed to electrons in the convoy emission region). According to the authors of the simulation [52], the origin of the overestimate binary electron emission intensity, could be due to an inaccurate description of the momentum density of the valence electrons. Because of the sensitivity of the binary shoulder to the wave function used to describe the surface valence electrons, measurements of binary electrons could provide a technique to obtain detailed information on the Compton profile of surface valence electrons.

Absolute yields of convoy electrons, obtained by integration of Eq. 26 over both the FWHM in electron energy and emission solid angle, are plotted in Fig.5.5 for incoming 3.6 MeV and 6.0 MeV C^{2+} projectiles. The absolute values of the convoy yields for ion-surface interactions are found to be much larger than those for ion-solid collisions. This is due to both the broad angular distribution of convoy electrons and the large effective path along the surface from which they originate. In contrast, convoy electrons from ion-solid collisions are produced over a short distance of the order of a free electron mean free path prior to exit [28].

Fig. 5.5 also shows the results of the CTMC simulation for the absolute yield. Considering the difficulties involved in the modeling of the complex dynamics of ion-surface collisions involving a large number of binary collisions, the agreement between the theoretical and experimental yields is quite good. The current level of agreement is comparable to that usually found in comparisons of absolute yields of electrons in the much simpler problem of intermediate-energy ion-atom collisions [53].

The yields shown in Fig. 5.5 decrease for increasing projectile velocity. In order to understand this velocity dependence, the separate contributions to convoy emission

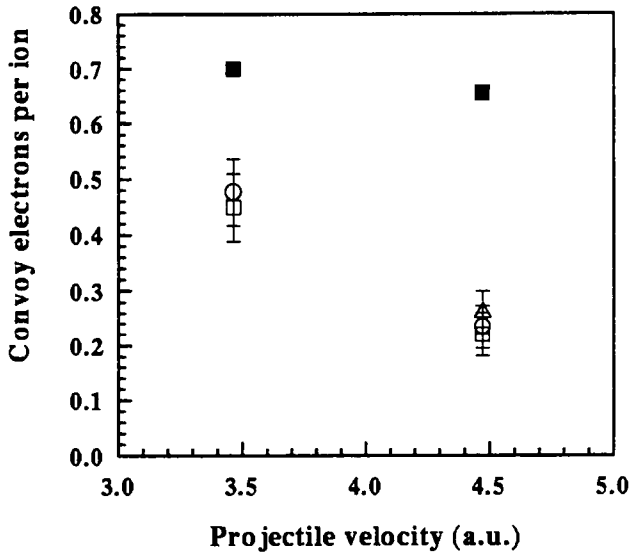

Figure 5.5: Experimental (hollow symbols) and theoretical (filled symbols) convoy electron yields for two projectile velocities. The various hollow symbols represent the yields measured for different exit charge states (squares for $q_{out} = 3$, circles for $q_{out} = 4$ and triangles for $q_{out} = 5$). The yields are obtained by integration over the FWHM in electron energy and over the angular regions employed in Fig. 5.4.

from electrons in different shells of the silicon target are displayed in Fig. 5.6. These yields have been calculated [52] ignoring charge state fluctuations leading to charge state equilibration. They are calculated assuming a fixed projectile charge equal to the mean exit charge state obtained from the measurements presented in connection with Fig. 4.11, and integrating the triply differential yield over a larger range of electron energies and angles than the FWHM. This considerably reduces the amount of computer time needed to obtain statistically accurate yields over a wide range of projectile velocities. In the present projectile velocity regime, i.e. between 3.5 a.u. and 4.5 a.u., both M- and L-shell electrons of silicon significantly contribute to convoy emission.

Convoy electrons originating from the target are produced via an electron capture

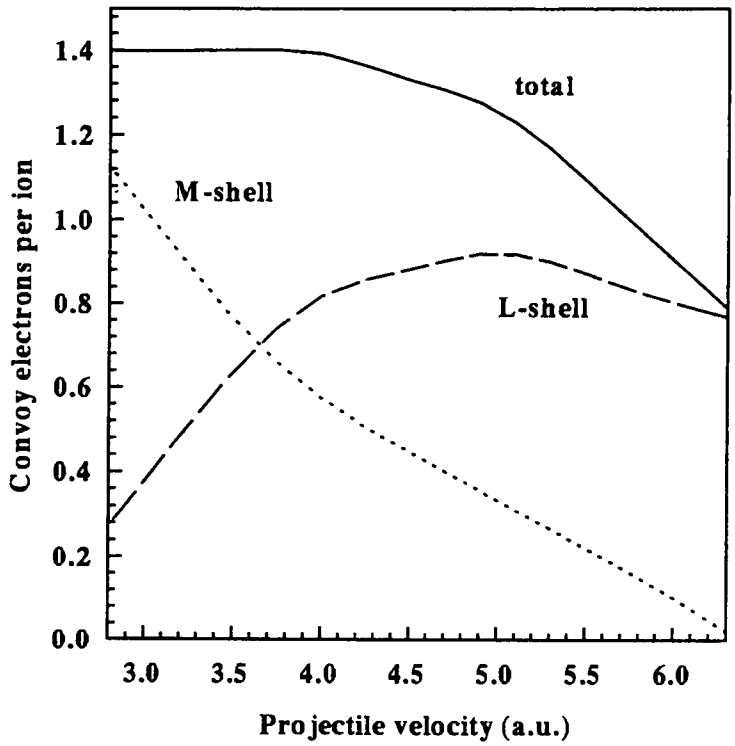

Figure 5.6: Theoretical prediction for convoy electron yield versus projectile velocity assuming a time and energy-independent projectile charge $q = 3$. Shown in the figure are the separate contributions from the M-shell (dotted-line) and L-shell (dashed-line) of silicon. The yield is calculated by integration over $E_{cusp} \leq E \leq 2E_{cusp}, 0° \leq \theta_x \leq 23°$, and $-11.5 \leq \theta_y \leq +11.5°$

process which populates bound or low-lying continuum states of the projectile. The projectile velocity dependence of the different contributions to Fig. 5.6 arises from the fact that the electron capture process is governed by the overlap of the momentum distributions of projectile and target states. The capture probability from a given shell maximizes when the velocity of the projectile is close to the average orbital velocity, v_{orb}, of the electron in the target state. This is the origin of the maximum of the yield of L-shell electrons near $v_{orb} \sim 4$ a.u.. The corresponding maximum for the M shell of Si is near $v_{orb} \sim 1$ a.u.. Therefore, for the projectile velocity range

of Fig. 8, the yield of M-shell electrons decreases as a function of projectile velocity, reflecting the high velocity tail of the initial electronic state, while still increasing for the L shell. The relative contribution of the different shells is also determined by two additional factors. First, the yield from a given shell is proportional to the number of electrons in it. Second, the cross sections for electron removal are proportional to the spatial size of a given shell, which is directly related to the binding energy of the electron. In comparison with previous calculations for SnTe surfaces, the ratio of the number of core to valence electrons in Si is smaller by a factor of 2 and the average size of the active core orbitals is a factor of 2 smaller. Thus, valence electrons should be expected to play a more important role for Si as compared to SnTe. The decrease of the experimental yields with projectile velocity agrees with this prediction.

5.4 Angular distributions of convoy and binary emission

As previously mentioned the present experimental setup permits measuring simultaneously the number of electrons $N(E, \delta E, \Omega, \delta\Omega)$ emitted in the interaction with emission energy E and emission solid angle Ω with $N(E, \delta E, \Omega, \delta\Omega)$ corresponding to a triply differential (in energy and two ejection angles) electron emission intensity. Electron spectra measured in this particular way have the advantage, as opposed to singly differential measurements, to observe the emission direction for electrons in different regions of the energy spectrum over the entire range of electron energies.

Fig. 5.7 shows doubly differential electron emission intensity spectra produced by C^{1+} ions incident at 0.15° on a silicon surface and with total kinetic energies of 3.6 and 6.0 MeV. The spectra are shown as contours of equal electron intensity, as seen by the PSD, as a function of the emission energy E and one of the two ejection angles i.e. θ_x. To obtain such spectra the triply differential electron emission intensity , $N(E, \delta E, \Omega, \delta\Omega)$, has been integrated over the FWHM of the angular distribution in the other ejection angle θ_y. As observed in the figure the main effects on the convoy peak *i.e.* the shift in energy and angle, are clearly observed. Interestingly electrons

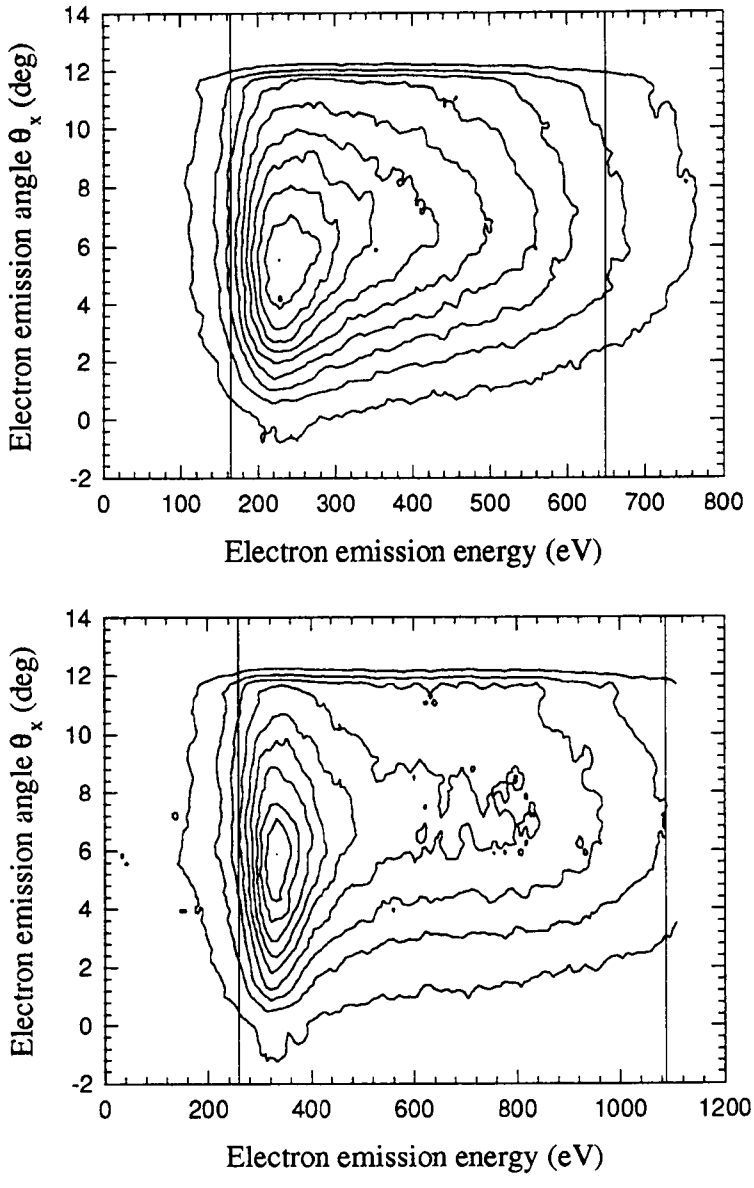

Figure 5.7: Doubly differential electron emission (in energy and ejection angle θ_x) intensity shown as contours of equal intensity and equally spaced between zero and the convoy peak rate. Spectra corresponds to C^{2+} ions incident upon a silicon surface at total kinetic energies of 3.6 MeV (top) and 6.0 MeV (bottom). The vertical lines at $E = \frac{v_P^2}{2}$ and $E = 2v_p^2$ indicate the position of the cusp and the zero degree binary encounter peak.

with energies higher than the accelerated convoy peak, E_{convoy} are emitted at even larger angles away from the surface than are the convoy electrons. The shape of the contours show that there is a smooth transition towards larger emission angles for increasing electron energy. This creates a depletion of events region closer to the surface for electron energies $E > E_{convoy}$. In other words the spectra shows that electrons with energies higher than E_{convoy} are pushed even further away from the surface.

The analysis of Fig. 5.7 discussed in the above paragraph indicates that the angular distribution of convoy electrons is shifted closer to the surface than the distribution of binary electrons. Fig. 5.7 also shows that the angular distributions of both convoys and binaries are very wide. In order to study if the shifted angular distributions leads to a separation of both structures, as seen in the energy spectrum, for any particular emission angle θ_x, the energy spectrum has been plotted for two angular regions as shown in Figs. 5.8 and 5.9. The first region corresponds to electrons emitted with angles in the range $1.5° < \theta_x < 4.5°$ while the second angular region are electrons emitted in the range $8.5° < \theta_x < 10.5°$. The energy spectra in Figs. 5.8, 5.9 have been obtained by integrating the spectra of Fig. 5.7 over the above angular regions and are shown in the angular distribution displayed on the bottom part of the figures. For both slices we see that the convoy and binary structures still overlap, however several interesting observations can be made. For the angular slice near the surface the convoy peak dominates over the binary shoulder for both projectile energies, indicating that convoys are emitted closer to the surface than are binary electrons. For both observation angles the intensity of the binary shoulder almost doesn't change. However the intensity of the convoy peak changes drastically being partially suppressed for larger angles.

In the previous section the origin of convoy and binary emission was studied by comparing measured and calculated electron spectra obtained by integrating the triply differential electron emission over the FWHM in the emission angles θ_x and

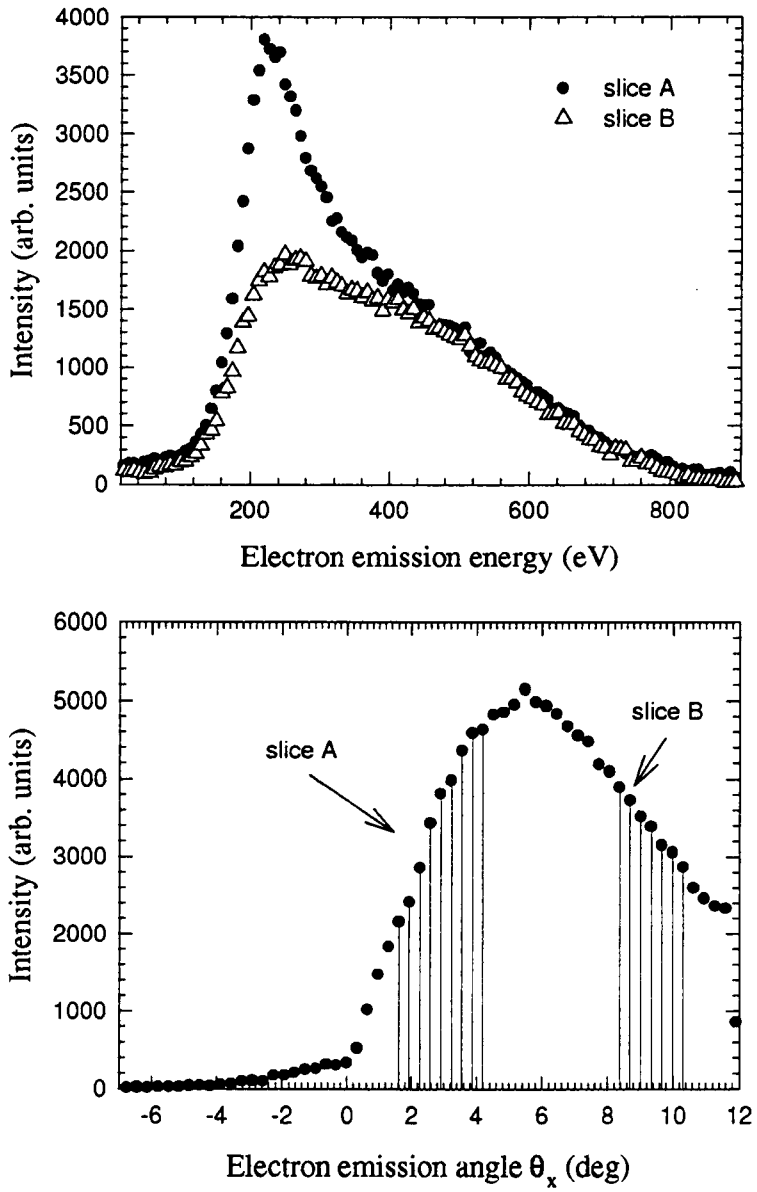

Figure 5.8: Top: Energy distributions produced by 3.6 MeV ions for two different slices in angle (see text) corresponding slice A to $1.5° \leq \theta_x \leq 4.5°$ (solid symbols) and slice B to $8.5° \leq \theta_x \leq 10.5°$ (hollow symbols). Bottom: Angular distribution of emitted electrons showing the chosen slices A and B

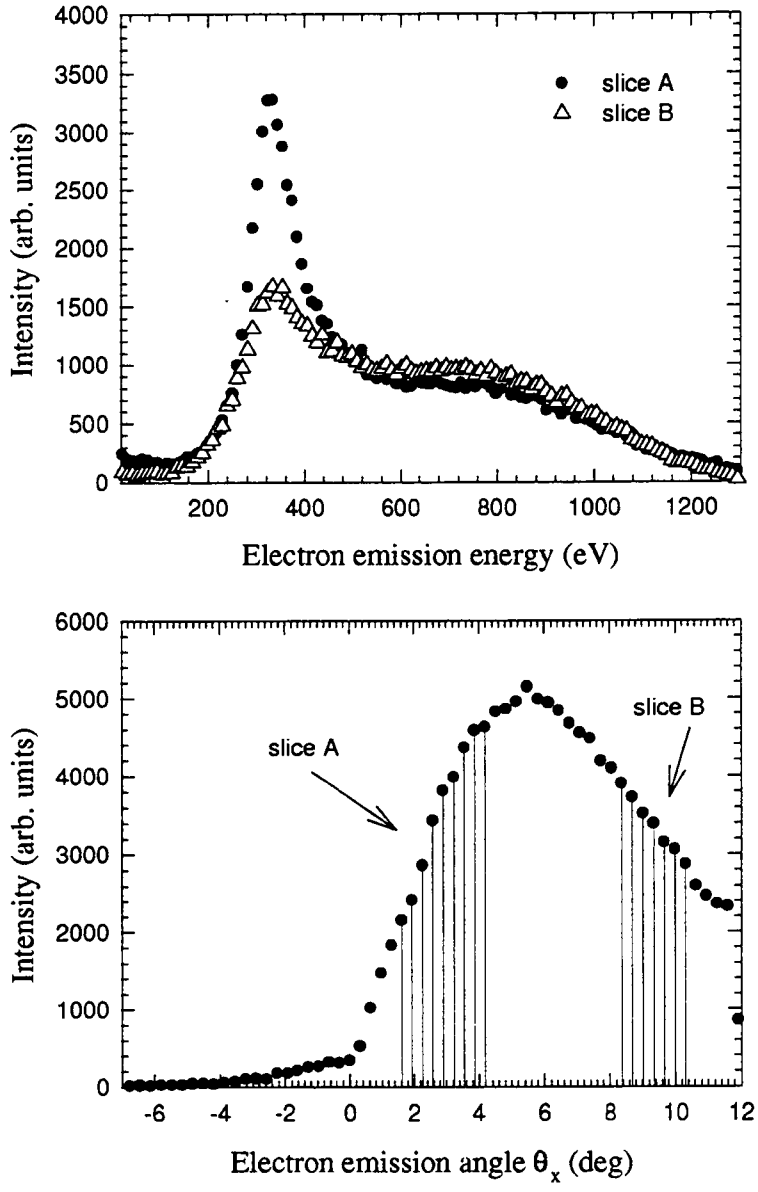

Figure 5.9: Energy and angular distributions of emitted electrons produced by 6.0 MeV ions. The angular slices are the same as in Fig. 5.8.

θ_y. It was concluded that convoy emission results from capture of core and valence electrons in the silicon target. It is not possible to separate the two contributions to the convoy peak in an experiment. In principle, the angle θ_x with which the electrons are ejected from the collision is determined primarily by the mechanism with which the electrons are emitted, e.g. *i.e.* ECC vs. binary encounter, rather than by the initial state from which they are emitted. Electrons captured from either valence or core states in the silicon target would in other words, be expected to have an angular distribution that peaks at a similar value of ejection angle θ_x. However, a detailed comparison between experimental and theoretical energy spectra, such as the ones shown in figures 5.8 and 5.9 obtained for different angular slices, may provide information about the relative contribution of valence and core electron emission to the convoy peak as a function of electron emission angle.

5.5 Dependence of the convoy peak shift with incident charge state

Another aspect of the convoy emission process which can be discussed from the data shown in Fig. 5.1 is the projectile velocity dependence of the convoy peak. In principle it would be expected that at the lower projectile velocities the interaction time between the emitted electron and the surface wake is larger resulting in a larger convoy peak shift. This trend is observed in figures 5.1 as the peak shift becomes smaller for larger projectile velocities. However the velocity dependence of the peak shift becomes a complicated problem when considering collision parameters other than the projectile velocity, in particular the projectile charge and the distance of closest approach of the ion to the surface. The dependence on the projectile charge has been studied [13] by measuring the convoy peak at two different projectile velocities and for varying incoming charge states

Fig 5.10 shows detailed electron emission spectra around the convoy peak pro-

duced by carbon ions in charge states $q = 1, 2, 3$, incident at a grazing angle of 0.2° and with kinetic energies of 3.6 and 6.0 MeV. The data is expressed as given by equation 27 by integrating the emission over the FWHM of the angular distribution. The peak shifts have been measured from the spectra shown in the figures and expressed as a fractional shift $\Delta E/E_{cusp}$ which has been plotted as a function of the incoming charge state of the projectile shown in Fig. 5.11 ($\Delta E = E_{convoy} - E_{cusp}$). As seen in the figure, an incoming charge state dependence is observed for the higher projectile velocity, while no charge state dependence is noticeable at the lower projectile velocity. For a projectile energy of 3.6 MeV, the convoy peak was invariably observed at 216 eV, amounting to a shift of 52 eV independent of the incident charge state to within the accuracy of the spectrometer energy calibration. However, in the case of 6 MeV projectiles, the shift was observed to be dependent on the initial projectile charge state: the convoy peak energy varies between 321 eV for C^{2+} ions and 332 eV for C^{4+} ions, corresponding to shifts between 47 and 58 eV, respectively. Deriving the singly-differential spectra from the triply-differential raw data sets using reasonably different integrations (for example, for θ_x integrated over the FWHM of the convoy peak vs. over the unobstructed angular field of view of the spectrometer) does not appreciably affect the peak positions and shifts; in fact, the plotting symbols displayed in Fig. 5.11 overlap the range of values obtained by several such choices of angular integrations.

The convoy electron acceleration, or peak shift, is governed by the amplitude of the surface wake potential and by the evolution thereof as that wake responds to changes in both position and charge state of the projectile. The projectile charge fluctuates during the course of the collision due to electron capture and loss processes. As shown in Fig. 4.7 the exiting ions achieve charge state equilibrium. The charge state independence of the peak shift at 3.6 MeV suggests that charge equilibration has been reached earlier in the collision. However for the faster projectiles (6.0 MeV) the complicated dependence observed indicates that the charge of the ion, at the time

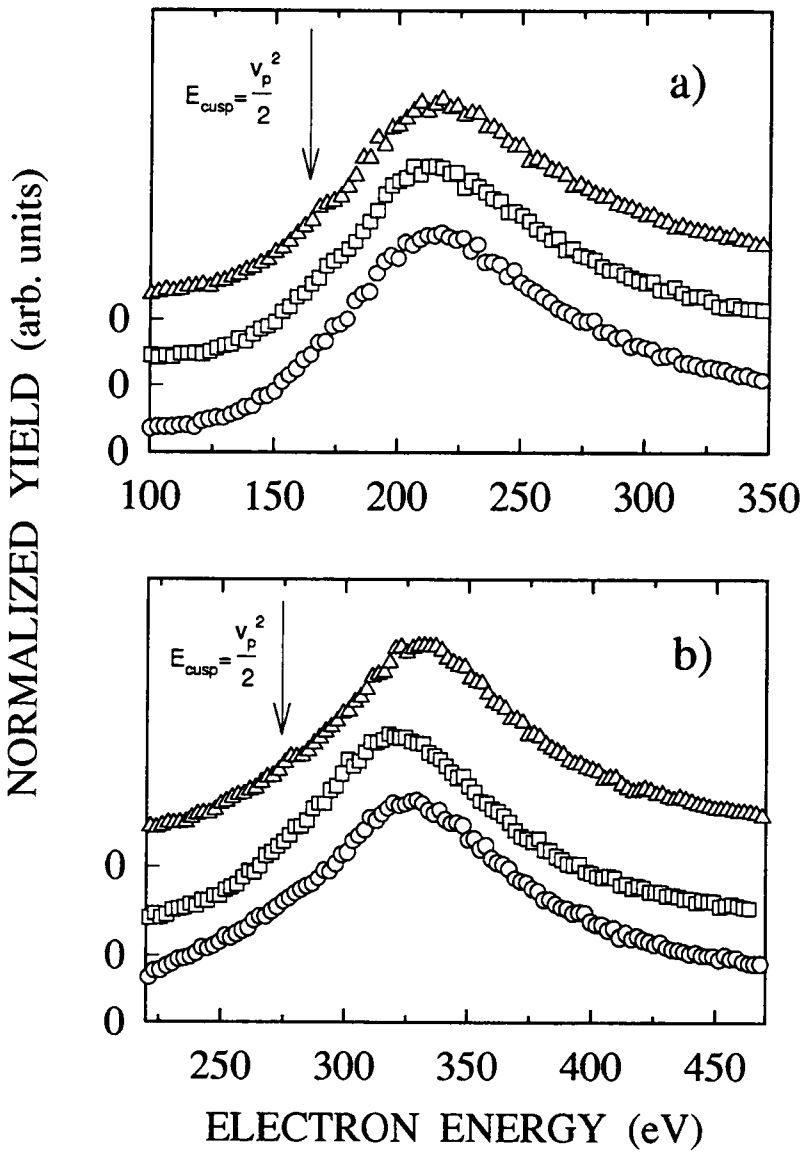

Figure 5.10: Detailed emission spectra for a) 3.6 MeV and b) 6.0MeV carbon ions with initial charge states 1+ (circles) 2+ (squares), and 3+ (triangles) incident at 0.2° upon a silicon(100) surface.

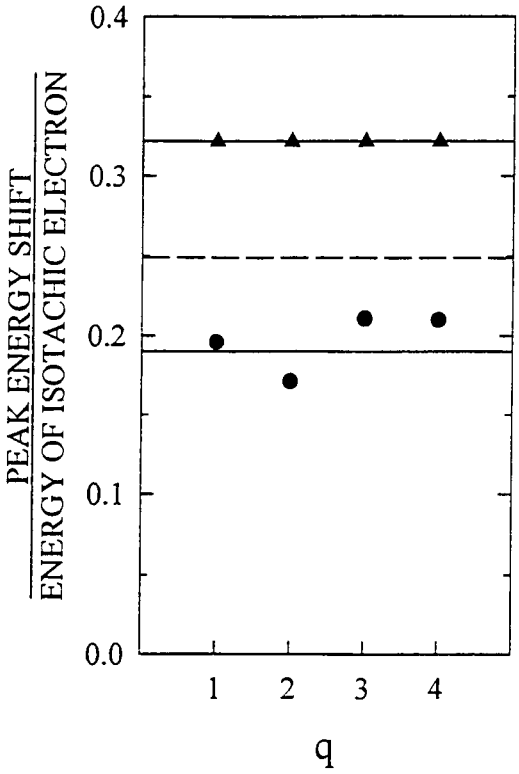

Figure 5.11: Dependence of the fractional shift of convoy peak energy, as defined in the text, upon incident charge state, q, and energy for 3.6 MeV (triangles) and 6.0 MeV (circles) projectiles. $1/v_p^2$ scaling of the peak shift, normalized to the 3.6 MeV data, would produce results clustered about the solid horizontal lines, whereas $1/v_p$ scaling would predict 6.0 MeV data clustered about the dashed horizontal line.

in the collision of maximum convoy production probability, is not fully equilibrated *i.e.* the mean charge at that time during the collision is not independent of the incoming charge.

Despite of the incoming charge state dependence observed the convoy yields result to be independent of the exiting charge states as discussed in connection with Fig. 5.5. Similarly the exit charge state distributions are independent of the incoming charge states. These observations suggest that after the convoys are produced, the ion still undergoes enough collisions to loose memory of its charge at the moment of maximum convoy emission probability.

The incoming charge state dependence makes the study of the velocity dependence of the convoy peak shift a complex matter. Nevertheless, it provides a good point of comparison with results obtained by Kimura *et al* [10] who used SnTe (100) surfaces. The data points for all incoming charge states and for the 3.6 MeV ions lie on a straight horizontal line, as seen in Fig. 5.11, corresponding to a fractional shift of $\Delta E/E_i = 0.32$. Scaling this value by $1/v_p$ from the 3.6 MeV projectile case to 6 MeV leads to a fractional shift of 0.25, as shown by the dashed horizontal line in Fig. 5.11, whereas $1/v_p^2$ scaling produces a value of 0.19, shown by the lower solid line in Fig. 5.11. On average, considering all incident charge states, the data seem to favor a $1/v_p^2$ scaling of $\Delta E/E_i$. A $1/v_p^2$ dependence is consistent with the result of Kimura et al. [10], who measured shifts of about 0.50 and 0.31 for 3.6 MeV C^{3+} and 6 MeV C^{4+} ions, respectively. The somewhat larger overall acceleration observed by them ($\Delta E/E_i \sim 0.31$, compared with our $\Delta E/E_i \sim 0.21$ for 6 MeV C^{4+}) is consistent with the higher Z_T of the constituent atoms of their SnTe surface, but may also reflect contributions from trajectory effects.

6 Summary

Incoming carbon ions with energies of approximately 0.5 MeV/amu were directed at grazing angles towards a silicon surface. Absolute electron emission spectra were obtained by measuring the emitted electrons in coincidence with carbon ions scattered in the specularly reflected direction $\theta_{out} = 2\theta_{in}$, and in a particular exit charge q_{out}. The main focus of this work has been the determination of the absolute yield of convoy electrons in grazing incidence ion-surface collisions. The observed value of the yield for the projectile velocity regime studied is ~ 0.4 electrons per ion integrated over the full-width at half maximum in energy and angle of the convoy peak structure. This value is found to be larger than typical values of convoy yields resulting from transmission foil experiments. This is consistent with the electrons originating over a large effective path length along the surface and is in contrast with observable convoys produced within a short distance of the exit surface in the case of ion-foil transmission experiments. By comparing the velocity dependence of the measured absolute yields with results obtained from a CTMC simulation [18] describing electron emission in grazing incidence ion-surface collisions, the origin of convoy emission has been addressed. The present measurements indicate that convoys result from capture of L- and M-shell electrons in the silicon target, corresponding to core and valence electrons respectively. This result is in contrast with previous conclusions [17, 18], derived from measurements employing SnTe surfaces, that convoy emission originates mainly from core states of the target. Combining the present results for Si surfaces with previous measurements using SnTe surfaces suggests that convoy emission in ion-surface collisions is sensitive to the target species.

Further analysis of the electron spectra leads to the following observations: (i) The convoy peak is shifted in energy and angle with respect to the position of the peak observed in the case of ion-atom collisions. The shift of the peak is due to the repulsion produced by the ion induced surface wake potential exerted on the

convoy electron. However, the same peak shift, is also observed under conditions in which the ions are expected to penetrate the surface, suggesting that the bulk-wake plays an important role in the acceleration of convoy electrons. (ii) The angular distributions of convoy and binary encounter electrons are shifted a few degrees away from the surface. Convoy electrons are emitted at smaller ejection angles θ_x than binary electrons.

In addition, angular and charge state distributions of carbon ions scattering from a silicon surface were obtained. The ion angular distributions indicate that in the regime of projectile velocities utilized and for angles of incidence $\theta_{in} \approx 0.15°$, the ions are scattered from the surface almost exclusively in the specular direction. Scattered ion charge state distributions, and corresponding exiting charge state fractions, are observed to be independent of the incoming charge state of the projectile. This indicates that the ions exiting the ion-surface interaction region achieve charge state equilibrium in this projectile velocity regime, similarly to what is known to happen with ions transmitted through thin foil targets.

References

References

[1] R. A. Baragiola, Nucl. Inst. and Meth. B **78**, 223 (1993).

[2] G. Spierings, I. Urazgil'din, P. A. Zeijlmans van Emmichoven, A. Niehaus, Nucl. Inst. and Meth. B **115**, 220 (1996).

[3] P. Varga and H. Winter, *Electron Emission II*, (Springer-Verlag, Berlin 1992).

[4] L. C. Feldman and J. W. Meyer, *Fundamentals of Surface and Thin Film Analysis* (North Holand, Amsterdam, 1986).

[5] L. Ferraris and R. Baragiola, Phys. Rev. A **33**, 4449 (1986).

[6] H. Winter, P. Strohmeier, and J. Burgdörfer, Phys. Rev. A **39**, 3895 (1989).

[7] M. Hasegawa, K. Kimura and M. Mannami, J Phys. Soc. Jap. 57, 1834 (1988).

[8] A. Koyama et al, Phys. Rev Lett. **65**, 3156 (1990); H. Ishikawa et al, Nucl. Inst. and Meth. B **67**, 160 (1992).

[9] T. Iitaka, Y. H. Ohtsuki, A. Koyama, and H. Ishikawa, Phys. Rev. Lett. **65** 3160 (1990).

[10] K. Kimura, M. Tsuji, and M. Mannami, Phys. Rev A **46**, 2618 (1992); Y. Mizuno, M. Hasegawa, Y. Susuki, K. Kimura, and M. Mannami, Nucl. Inst. and Meth. B **67**, 164 (1992).

[11] E. A. Sánchez, O. Grizzi, M. L. Martiarena, and V. H. Ponce, Phys. Rev. Lett. **71**, 801 (1993); E. A. Sánchez, M. L. Martiarena, O. Grizzi, and V. H. Ponce, Phys. Rev. A **45**, R1299 (1992).

[12] G. R. Gomez, E. A. Sanchez, O. Grizzi, M. L. Martiarena, V. H. Ponce, Nucl. Inst. and Meth. B **122**, 171 (1997).

[13] H. Lebius, R. Minniti, J. Y. Lim, and S. B. Elston, Phys. Rev. A **54**, 4171 (1996).

[14] R. Minniti, S. B. Elston, C. O Reinhold, J. Y. Lim, J. Burgdörfer, (submitted for publication in Phys. Rev. A).

[15] J. Burgdörfer, Nucl. Inst. and Meth. **24/25**, 139 (1987).

[16] A. Koyama, Nucl. Instr. and Meth. bf B67 103 (1992).

[17] C. O. Reinhold, J. Burgdörfer, K. Kimura, and M. Mannami Phys. Rev. Lett. **73**, 2508 (1994).

[18] C. O. Reinhold and J. Burgdörfer, Phys. Rev A **55**, 450 (1997).

[19] U. Thumm, J. Phys. B: At. Mol. Opt. Phys. **25** 421 (1992).

[20] M. L. Martiarena, E. A. Sanchez, O. Grizzi and V. H. Ponce, Phys. Rev. A **53**, 895 (1996).

[21] C. O. Reinhold, J. Burgdörfer, R. Minniti, and S. B. Elston, Nucl. Instrum. and Meth. **B** 124 320 (1997).

[22] J. Y. Lim, Ph.D. Dissertation, University of Tennessee, 1996 (unpublished).

[23] J. Burgdörfer, *Review of Fundamental Processes and Applications of Atoms and Ions*, ed. C.D. Lin (World Scientific, Singapore 1993).

[24] Yoshi-Hiko Ohtsuki, *Charged beam interaction with solids*, (Taylor and Francis Inc., New York, 1983), sections 6.4 and 7.5.

[25] P. M. Echenique, F. Flores, and Ritchie, in *Solid State Physics*, edited by H. Ehrenreich and D. Turnbull (Academic, San Diego, 1990), Vol. 43, p.230.

[26] F. J. García de Abajo and P.M. Echenique, Phys. Rev. B **46**, 2663 (1992).

[27] Figures kindly provided by Carlos Reinhold.

[28] M. Breinig, S. B. Elston, S. Huldt, L. Liljeby, C. R. Vane, S. D. Berry, G. A. Glass, M. Schauer, I. Sellin, G. D. Alton, S. Datz, S. Overburry, R. Laubert, M. Suter, Phys. Rev. A **25**, 3015 (1982).

[29] Hans A. Bethe and Edwin Salpeter, *Quantum Mechanics of one and two electron atoms* (Plenum Rosetta eds. 1977).

[30] J. Burgdörfer, M. Breinig, S. B. Elston, and I. Sellin, Phys. Rev A **28** 3277 (1983) and references 1,2,3 therein.

[31] H. Goldstein, *Classical Mechanics, second edition* Addison Wesley, Massachusetts (1980)

[32] D. H. Lee, P. Richard, T. J. M. Zourus, J. M. Sanders, J. L. Shinpaugh, and H. Hidmi, Phys. Rev. A **41** 4816 (1990).

[33] M. L. Martiarena, E. A. Sanchez, O. Grizzi and V. H. Ponce, Nucl. Instrum and Meth. **B** 90, 300 (1994).

[34] The silicon wafers were provided by Texas Instruments.

[35] B. S. Swartzentruber, Y. -W. Mo, M. B. Webb, and M. G. Lagally, J. Vac. Sci. Technol. A, Vol.7 2901 (1989).

[36] G. Ertl and J. Kuppers, *Low Energy Electrons and Surface Chemistry* (VCH Publishers, Florida (1985)).

[37] Kenneth D. Sevier, *Low Energy Electron Spectrometry*, (John Wiley, New York 1972).

[38] Co-netic AA sheets (0.014 inches thick) were used obtained commercially from Magnetic Shield Corporation. These sheets are stress annealed to be able to machine the material and still mantain its magnetic shielding characteristics.

[39] Designed by Stuart B. Elston.

[40] Y. Fujii, K. Kishine, K. Narumi, K. Kimura and M. Mannami, Phys. Rev A **47**, 2047 (1993).

[41] V. P. Zaikov, E. A. Kral'kina, N. F. Vorobjev, I. S. Dimitriev, V. S. Nikolaev and Ya. A. Teplova, Nucl. Instrum. and Meth. **B5** 10 (1984).

[42] A. B. Wittkower and H. D. Betz, Atomic Data **5**,113-166 (1973).

[43] K. Shima, T. Mikumo, and H. Tawara, Atomic Data and Nuclear Data Tables, **34**, 364 (1986).

[44] H. D. Betz, Rev. Mod. Phys.,**44**, 465 (1972).

[45] W. Meckbach, I. B. Nemirovsky, and C. Garibotti, Phys. Rev. A **24** 1793 (1981).

[46] S. D. Berry, G. A. Glass, I. A. Sellin, K.-O. Groenveld, D. Hofmann, L. H. Andersen, M. Breinig, S. B. Elston, P. Engar, M. M. Schaur, N. Stolterfoht, H. Schmidt-Böcking, G. Nolte, and G. Schiwietz, Phys. Rev. A **31**, 1392 (1985).

[47] R. DeSerio, Rev. Sci. Instrum. **60**, 381 (1989).

[48] Joseph Ladislas Wiza, Nucl. Instrum. and Meth., **162**, 587 (1979).

[49] K. Kimura, T. Kishi, and M. Mannami, Nucl. Inst. Meth. B **90**, 282 (1994).

[50] M. -C. Desjonquéres and D. Spanjaard, *Concepts in Surface Physics* , ed. G. Ertl, R. G. Gomer, and D. L. Mills (Springer-Verlag, Berlin 1993).

[51] J. A. Appelbaum and D. R. Hamann, Rev. Mod. Phys., **48**, 479 (1976).

[52] The calculations associated with figures 5.4, 5.5 and 5.6 have been performed by Carlos Reinhold and Joachim Burgdörfer as well as various of the related discussions.

[53] P. D. Fainstein, V. H. Ponce, and R. D. Rivarola, Journal Phys. B **24**, 3091 (1991).

Vita

Ronaldo Minniti was born in New Bedford, Massachusetts. He attended the University of Buenos Aires in Buenos Aires, Argentina and graduated in July 1991 with a degree of Licenciate (Masters) in Physics. In the fall of 1991 he entered the Graduate School of the University of Tennessee, Knoxville. He has worked since the fall of 1992 on the pursue of his Doctor of Philosophy degree with a major in Physics under the supervision of Dr. Stuart Elston studying the interaction of ions with surfaces, and has in addition collaborated with other members of the atomic physics group at the University of Tennessee.

Ronaldo received a Doctor of Philosophy degree in Physics in the fall of 1997. He has accepted a National Research Council Associateship to work at the National Institute of Standards and Technology.